TEM Cell design for `Material Characterization`

Edward Lindenholst
`elt11ejo@student.lu.se`

Filip Olsson
`elt11fol@student.lu.se`

Department of Electrical and Information Technology
Lund University

Advisor: Christer Larsson
Advisor: Torleif Martin
Examinator: Mats Gustafsson

October 3, 2016

Abstract

This thesis investigates a TEM cell (Transverse ElectroMagnetic cell) design for material characterization. The focus is to design a practical setup where the material measurement is straightforward to implement. A test sample is placed between the two ports in the setup to measure the scattering parameters. The impedance matching between the coaxial to microstrip transition and the TEM cell tapering are investigated. The TEM cell operating bandwidth is $0 - 5GHz$. The design is simulated and optimized in CST (Computer simulation technology) and is manufactured and measured with a network analyzer to verify its performance. From the measured scattering parameters two different algorithms are investigated to extract the permittivity of the sample. Finally it is concluded that the measurements are in a good agreement with the numerical simulations and that the TEM cell works well for measuring low permittivity materials.

Acknowledgments

Table of Contents

List of Figures

List of Tables

Chapter 1

Introduction

This project aims to explore alternative material characterization measurement setups using a TEM cell (Transverse ElectroMagnetic cell) that complements and also simplifies material measurements [1, 2, 3, 4, 5, 6, 7, 8]. The project is carried out at Saab which is one of Sweden's most technology-intensive companies working in the defense sector. Saab's work with avionics, radar applications and stealth technology sets high demands on the knowledge of how the electrical and magnetic fields behave due to variations of permittivity and permeability of different materials. A typical application where the knowledge of the permittivity and permeability is of interest, is when designing materials for fighter jets shown in Fig. 1.1.

Figure 1.1: Jas 39 Gripen, from [43].

Material characterization is a complex and interesting science and the determination of the material properties at microwave-frequencies is challenging. Information about the permittivity and permeability is of interest in a variety of applications, for example in the communication and military industry. By applying an external electromagnetic field on a material sample, material properties can be investigated. To determine how much impact a material has on an electromagnetic

field, one needs to determine the constitutive relations of the material. The permittivity ϵ and the permeability μ are associated with the electric and magnetic fields, respectively. Behind the two parameters there are physical explanations which are treated in the following chapters.

The basic principle for determining the permittivity and the permeability is to measure the reflected and transmitted electromagnetic fields when a material sample is illuminated with an incident electromagnetic field, as shown in Fig. 1.2. This can be done using a free space measurement setup with antennas or by using guided waves in a waveguide [9].
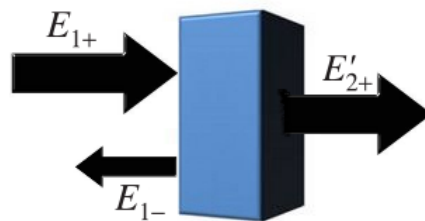
Figure 1.2: Dielectric slab where E'_{2+} is the transmitted electric field from the incident E_{1+}, and E_{1-} is the reflected electric field.

There is a wide range of techniques used today to determine the constitutive relations, and depending on the desired frequency range one needs to consider different kinds of waveguides with specific operating bandwidths. To determine the operating bandwidth for a waveguide one needs to consider which modes the system support. The *cutoff frequency* determines the frequency at which a mode can propagate and depends on the transverse (orthogonal to the propagation direction) components [9]. The lower limit of the operating bandwidth is defined by the *cutoff frequency* of the first propagating mode and the upper limit is determined from the *cutoff frequency* of the first higher order mode.

The first mode that can propagate in the system is defined as the lowest propagating frequency. This means that the *cutoff frequency* for the first mode is the lowest frequency where you can transfer a signal with information in the propagation direction without that the information get lost due to attenuation, from the transmitter to the receiving point in the waveguide. Waveguides also support higher order modes and two modes can simultaneously propagate in the waveguide. This phenomena is not desirable because one can not determine which mode is carrying the information and the modes can interfere with each other.

One method used today is the parallel plate capacitor where the permittivity can be determined for a fixed frequency [10, 11]. This method works good for a few frequencies, but gets time consuming while measuring over a larger spectrum. That is when the rectangular waveguide comes into the picture. The rectangular

waveguides can be used to determine the permittivity and the permeability for a given frequency range [12]. The advantages of this method is that it is easy to insert a test sample and it generates accurate measurements. This method is a one-conductor system and does only support the TE and TM mode with *cutoff frequency $f_c > 0$*, which is undesired for lower frequency measurements. Waveguides that support TEM modes have the specific characteristic that the lower *cutoff frequency* is zero [9], which means that they theoretically works for measurements from DC.

Two-conductor systems, for example the coaxial waveguide, support TEM modes. The coaxial waveguide has some disadvantages. The test sample is difficult to insert into the waveguide and it needs to be perfectly fitted inside the setup to avoid measuring errors due to field leakage. Another problem is to know exactly where the sample is located within the waveguide, which is important for the calibration where you move the reference plane to the test sample's surface. To avoid the disadvantages of the rectangular waveguide where the fundamental modes are the TE or TM mode, a two-conductor system is investigated [13, 14, 15]. A microstrip based TEM cell has the advantages that it excites a TEM mode and that the samples are easy to insert in the TEM cell. The test sample does not need the same precision of size and shape when manufactured as the case is for the coaxial line setup.

In this thesis a TEM cell is theoretically investigated, designed and manufactured for material characterization. It is similar to the ideas based on the parallel plate waveguide [10, 11, 13]. The fundamental mode for the waveguide is the TEM mode, but the TE and TM modes can also be triggered by the waveguide. The operating bandwidth is determined from the higher order TE or TM modes [16]. Scattering parameters are used to extract material characteristics. The design is investigated in CST, a numerical FDTD solver [17]. The setup is designed to match a 50Ω system.

Two different algorithms, Baker Jarvis [18] and Nicolson-Ross-Weir [19] are used to calculate the complex permittivity and permeability for the test sample in the microstrip waveguide [20]. The test sample consist of teflon because of its well-known electromagnetic properties that are defined for a wide range of frequencies.

Chapter 2 serves as an introduction to material physics. Chapter 3 highlights the fundamentals of electromagnetism and further on dives into the applications of electromagnetic waves and how they behave in waveguides and transmission lines, including different types of impedance matching techniques. Chapter 4 is an introduction to scattering parameters and the simulation and measuring tools. From the information gained from the first 4 chapters, the final design is motivated and simulated in chapter 5. Chapter 6, 7 and 8 presents the manufactured TEM cell, validation and verification of this project, respectively.

Chapter 2

Material Characterization

Electromagnetic properties of materials are of interest for scientists as well as for people working with applications. There are 102 known elements from which 92 can be found in nature [21]. All matter is formed from either one or a combination of the different elements. An atom consist of protons (positive charged), neutrons (neutral charge) and electrons (negative charge), which can be seen from Bohr atom model of a water molecule in Fig. 2.1.
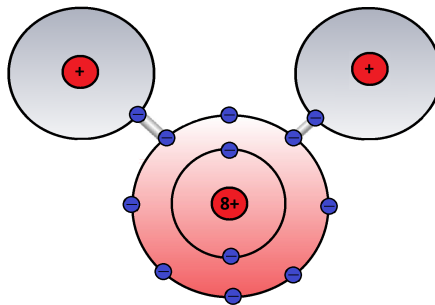
Figure 2.1: Bohr Atom-model of water molecule.

Every element has a number in the periodic system, Fig 2.2, defined from the number of protons in the atom.

Figure 2.2: Periodic System from [44].

Illuminating a material sample with an external electromagnetic field at for example microwave frequency, makes the material change the electromagnetic field pattern. The displacements of the electromagnetic field pattern is related to the permittivity and permeability. To characterize the permittivity and permeability of a materiel sample the electric and magnetic field are measured, respectively.

2.1   Dielectric Materials

Materials were the charges are not free to travel like in conductors, are named dielectric materials. As an ideal dielectric material has the special characteristic that it does not contain any free charges and is microscopically neutral as shown in Fig. 2.3.

Figure 2.3: Hydrogen atom.

Applying an external E-field to a dielectric material makes the bound charges move slightly relative to each other meaning that the centroids of the charge distribution shift slightly from the initial positions. In a perfect conductor on the other hand which only contains free charges,the free charges moves the surface of the material. The movement of the centroids relative to its initial state in the

atom creates numerous electric dipoles. Movement due to an applied external field of the small group of dielectric dipole in a material is called *polarization* [21]. *The polarization* due to the electric field alters the ability of the material to store electric energy. It is analogous to the potential energy stored in a spring stretching it a length from its initial state. There are three kinds of *polarization*; dipole or orientational *polarization*, where the dipole tends to align with the applied field, ionic or molecular *polarization* that contains positive and negative ions which displaces themselves due to the applied field. The third and the last *polarization* type is named electronic *polarization* and is the most usual behavior of material where the applied field displaces the electric cloud center of the atom relative to the center of the nucleus. The *polarization* phenomena gives rise to the potential energy stored in the material. To determine the static permittivity, a simple parallel plate conductor can be used. By determining the *polarization* vector **P** with the test sample between the parallel plate conductor and relate it to the case where the conductor contains only vacuum, the relative permittivity is defined in Eq. (2.1) [21].

$$\epsilon_{sr} = \frac{\epsilon_s}{\epsilon_0} \tag{2.1}$$

Where $\epsilon_0 = 8.854 \cdot 10^{-12}[F/m]$ is the permittivity in vacuum and ϵ_s is the measured permittivity of the sample. The relative permittivity ϵ_{sr} defines the charge storage capacity of a dielectric material relative to vacuum.

2.2   Magnetic Materials

A material with magnetic characteristics displays magnetic polarization when the material is exposed to an external magnetic field. It is not trivial to examine and understand the macroscopic behavior of magnetic material where quantum theory is applied. In this thesis we only treat dielectrics and will only mention that the relative permeability is defined as [21]

$$\mu_{sr} = \frac{\mu_s}{\mu_0} \tag{2.2}$$

where μ_0 is the permeability in vacuum and μ_s is the measured permittivity of the sample.

2.3   Complex Permittivity and Permeability

To determine the permittivity of dielectric materials where the frequency dependence is considered, the complex permittivity is defined as

$$\epsilon = \epsilon\prime - j\epsilon\prime\prime \tag{2.3}$$

Complex permittivity is written with a real part and an imaginary part. The real part $\text{Re}(\epsilon) = \epsilon\prime$ gives the relative permittivity of the dielectric material while

the imaginary part $\text{Im}(\epsilon) = \epsilon''$ defines the losses of the material. The effective electric losses are sometimes given as the electric loss tangent. The electric loss tangent is defined by

$$\tan \sigma_e = \frac{\epsilon''}{\epsilon'} \tag{2.4}$$

The complex permeability is defined in a similar way.

$$\boxed{\mu = \mu' - j\mu''} \tag{2.5}$$

There are different kinds of magnetic materials. Diamagnetic, paramagnetic and antiferromagnetic materials almost have the same relative permeability as vacuum μ_0. But for material with high permeability for example ferromagnetic and ferrimagnetic materials there is a loss tangent introduced. The loss tangent is a measure of the magnetic losses and is described by Eq. (2.6).

$$\tan \sigma_m = \frac{\mu''}{\mu'} \tag{2.6}$$

2.4 Transmission/Reflection Method to estimate material parameters

There are a range of different techniques to determine the material parameters such as, reflection methods, transmission/reflection methods, resonator methods and planar-circuit methods (just to name a few) [11, 22, 23]. The method used in this project is the transmission/reflection method. To determine the permittivity and/or permeability of the test sample, the material is placed in a waveguide fixture (for example in a coaxial line or in a microstrip line) and the scattering parameters are measured. To determine the material parameters, the scattering parameters are inserted in an algorithm where the required information is extracted and the desired material parameters are derived. There are several methods to determine the material parameters because when performing the transmission and reflection method the system of equations is generally over-determined. Two different methods, Nicolson-Ross-Weir [19] and Baker Jarvis [18] are examined and applied in this project.

2.4.1 Nicolson-Ross-Weir Algorithm

To explicitly determine the permittivity and permeability the Nicolson-Ross-Weir algorithm [19, 22] can be used. The algorithm uses the scattering parameters where both the measured reflection S_{11} and transmission S_{21} parameters are used [19]. Γ is the reflection coefficient which can be described by

$$\Gamma = K \pm \sqrt{K^2 - 1} \tag{2.7}$$

where

$$K = \frac{(S_{11}^2 - S_{21}^2) + 1}{2S_{11}} \tag{2.8}$$

To determine the sign of Eq. (2.7), gamma is required to be $|\Gamma| \leq 1$. The transmission coefficient T is defined by

$$T = \frac{(S_{11} - S_{21}) - \Gamma}{1 - (S_{11} + S_{21})\,\Gamma} \tag{2.9}$$

By using the equation above the permittivity ϵ and the permeability μ are described by Eq. (2.10) and (2.11) respectively.

$$\mu_r = \frac{1 + \Gamma}{(1 - \Gamma)\,\Lambda\sqrt{\frac{1}{\lambda_0^2} - \frac{1}{\lambda_c^2}}} \tag{2.10}$$

$$\epsilon_r = \frac{\lambda_o^2}{\mu_r \left(\frac{1}{\lambda_c^2} - \frac{1}{\Lambda^2}\right)} \tag{2.11}$$

where λ_c is the *cutoff wavelength* of the transmission line. λ_0 is defined as the *free space wavelength* in vacuum. Λ is defined by

$$\frac{1}{\Lambda^2} = -\left[\frac{1}{2\pi D}\ln\left(\frac{1}{T}\right)\right] \tag{2.12}$$

where D is the thickness of the sample.

The phase shift needs to be taken into account for the algorithm to work properly, because of the distance between the excitation point and the material placement. This can be done by calibrating to the reference plane and calculating the phase shift and assuming that the phase shift between every two frequency points consecutive is less than 2π [19].

2.4.2 Baker Jarvis

Depending on the type of waveguide fixture used, the scattering parameters have an important role in determining the material parameters. For waveguides with a certain reflection parameter over a measured frequency range, the reflection coefficient can interfere with the measurement resulting in inaccurate permittivity and permeability. The problems of the Nicolson-Ross-Weir algorithm is to compensate for the phase delay and that it does not work well for frequencies where the test sample length is a multiple of a half a wavelength [22]. For frequencies where the material thickness is a multiple of half a wavelength, the scattering parameter $|S_{11}|$ becomes almost zero and the algorithm gets algebraically unstable. Baker Jarvis is an algorithm where the transmission parameters S_{21} and S_{12} are taken into account and the reflection parameters S_{11} and S_{22} can be weighted with α, depending on the accuracy of the input data. Baker Jarvis, Eq. (2.13), is

an iterative algorithm [22, 24, 25] where the sample length and the position of the reference plane needs to be accurately known.

$$\frac{1}{2}\left[(S_{12} + S_{21}) + \alpha\,(S_{11} + S_{22})\right] = \frac{T\left(1 - \Gamma^2\right) + \alpha\Gamma\left(1 - T^2\right)}{1 - P^2\Gamma^2} \qquad (2.13)$$

α is a weighting factor and can be adjusted depending on the loss factor of the material. The propagating term with calibration of the reference plane, $P = e^{-jk_m d}$, where $k_m = k_0\sqrt{\epsilon_r \mu_r}$ and d is the thickness of the test sample. For a low loss material, α can be set to zero because the transmission parameter S_{21} is good. In general, the uncertainty of the method increases for high loss materials.

Chapter 3

Waveguide Theory

Classical electromagnetic theory describes the electric and magnetic phenomena in nature. *James Clerk Maxwell* (1831-1879) used four fundamental equations (3.1) to describe all electromagnetic phenomena in an accurate and elegant way [9, 26, 27].

$$
\begin{aligned}
\nabla \times \mathbf{E} &= -\frac{\partial \mathbf{B}}{\partial t} \\
\nabla \times \mathbf{H} &= \mathbf{J} + \frac{\partial \mathbf{D}}{\partial t} \\
\nabla \cdot \mathbf{D} &= \rho \\
\nabla \cdot \mathbf{B} &= 0
\end{aligned}
\qquad \textit{Maxwell's equations} \qquad (3.1)
$$

The *electric field* $\mathbf{E}$ and the *magnetic field* $\mathbf{H}$ are measured in [Volt/m] and [Ampere/m], respectively. *Electric flux density* $\mathbf{D}$ and the *magnetic flux density* $\mathbf{B}$ are measured in [Coulomb/m^2] and [Weber/m^2] or [Tesla]. *Electric displacement* and *magnetic induction* is another word for $\mathbf{D}$ and $\mathbf{B}$. The two last quantities are the *volume charge density* ρ and the *electric current density* measured in [Coulomb/m^3] and [Ampere/m^2], respectively [21].

Maxwell unified observations made by *Michael Faraday* (1791-1867), *Karl Fried-rich Gauss* (1777-1855) and *Andre-Marie Ampere* (1775-1836). *Maxwell* completed *Ampere's law* with the displacement current $\partial \mathbf{D}/\partial t$ which is fundamental to prove the existence of propagating electromagnetic waves. *Maxwell* realized that to preserve the *law of charge* conservation the displacement current was the missing ingredient to interlink the four equations together [9]. To derive *Maxwell's displacement current* the divergence is taken of both sides of *Ampere's law* and by using *Gauss's law* (3.2) and the vector identity (3.3)

$$
\nabla \cdot \nabla \times \mathbf{H} = 0 \tag{3.2}
$$

and

$$
\nabla \cdot \mathbf{D} = \rho \tag{3.3}
$$

we obtain:

$$\nabla \cdot \nabla \times \mathbf{H} = \nabla \cdot \mathbf{J} + \nabla \cdot \frac{\partial \mathbf{D}}{\partial t} = \nabla \cdot \mathbf{J} + \frac{\partial}{\partial t} \nabla \cdot \mathbf{D} = \nabla \cdot \mathbf{J} + \frac{\partial p}{\partial t}$$

and by using the vector identity from Eq. (3.2), the *law of charge* conservation is derived.

$$\frac{\partial \rho}{\partial t} + \nabla \cdot \mathbf{J} = 0 \qquad \textit{charge conservation} \qquad (3.4)$$

The charge conservation is an important law which is always true for a closed system. An analogy to charge is energy where energy cannot disappear or be created out of nothing. Energy can only transform into different kind of energy forms. The same applies to charge, it can not vanish or be created from nothing. Charge varies in regions of space because it travels between different regions. The *law of charge* conservation also states that charges in good conductors almost instantaneous move to the surface of the conductor and distribute itself to reach charge equilibrium at the surface of the structure[27].

3.1   Constitutive relations

Applying an electric or magnetic field to different kind of materials changes the electric and magnetic field pattern [21]. The constitutive parameters of linear materials are not a function of the applied field, otherwise they are nonlinear materials. Many materials have linear characteristics as long as the applied fields are within certain limits. When the constitutive parameters are not a function of position, the media is called homogeneous and otherwise in-homogeneous. All media have some degree of non-homogeneity, but if small, they are seen as homogeneous. Dispersive media is the case when the constitutive parameters depends on the frequency. When the constitutive parameters vary with the direction of the applied field the media is called non-isotropic otherwise it is called isotropic[21]. There exists a fundamental connection between the electric $\mathbf{D}$ and magnetic $\mathbf{B}$ flux densities which is related to the electric field $\mathbf{E}$ and magnetic field $\mathbf{H}$ respectively. Eq. (3.5) and Eq. (3.6) gives the relation between flux and field intensities in vacuum [9].

$$\mathbf{D} = \epsilon_0 \mathbf{E} \qquad\qquad (3.5)$$
$$\mathbf{B} = \epsilon_0 \mathbf{H} \qquad\qquad (3.6)$$

ϵ_0 is the permittivity of free space measured in $[Farad/m]$ and μ_0 is the permeability of free space measured in $[Henry/m]$. The physical constants have the numerical values:

$$\epsilon_0 \approx 8.854 \cdot 10^{-12} F/m \qquad\qquad (3.7)$$
$$\mu_0 = 4\pi \cdot 10^{-7} H/m \qquad\qquad (3.8)$$

By having the permittivity and permeability defined in vacuum two important constants can be derived, namely the speed of light and the characteristic impedance of vacuum.

$$c_0 = \frac{1}{\sqrt{\epsilon_0 \mu_0}} m/s \tag{3.9}$$

$$\eta_0 = \sqrt{\frac{\mu_0}{\epsilon_0}} \approx 377\Omega \tag{3.10}$$

3.2 Waveguides

Maxwell proved the existence of propagating electromagnetic waves. Electromagnetic waves can propagate in different media for example in free space using an antenna as a radiation element. Guided waves in a structure can be used to transfer energy with low losses, this kind of guides are called *waveguides*. There are different kinds of waveguides, and they have all different kinds of characteristics depending on the structure. Marcuvitz's [28] book provides a basic understanding of the waveguides and describes the theory in a mathematical way. The kind of mode a specific type of waveguide can transfer is determined from the cross section transverse to the propagation direction.

Deriving *Maxwell's* equation with respect to the propagation direction which often is defined as the z-direction, the electric and magnetic field are in the form [9]

$$\mathbf{E}(x,y,z,t) = \mathbf{E}(x,y)e^{j\omega t - j\beta z} \tag{3.11}$$

$$\mathbf{H}(x,y,z,t) = \mathbf{H}(x,y)e^{j\omega t - j\beta z} \tag{3.12}$$

Decomposition in the z direction gives Eq. (3.11) and Eq. (3.12) were β is the *propagation wave-number* along the structure. β can be defined in terms of speed of light in vacuum c_0 and angular frequency ω from

$$\beta = \frac{1}{c_0}\sqrt{\omega^2 - \omega_c^2} \tag{3.13}$$

where ω_c is the *cutoff frequency*.

Electromagnetic waves can travel long distances in space, *Maxwell's equation* can be rewritten in source free region of space [9] to

$$\begin{aligned} \nabla \times \mathbf{E} &= -\frac{\partial \mathbf{B}}{\partial t} \\ \nabla \times \mathbf{H} &= \frac{\partial \mathbf{D}}{\partial t} \\ \nabla \cdot \mathbf{D} &= 0 \\ \nabla \cdot \mathbf{B} &= 0 \end{aligned} \tag{3.14}$$

The Fourier transform of the derivative gives the relation $j\omega \Leftrightarrow \frac{\partial}{\partial t}$. Combining the Fourier transform of a derivative and the constitutive relations (3.5) and (3.6), Eq. (3.15) can be described by *Maxwell's equation* at a source-free region:

$$\nabla \times \mathbf{E} = -j\omega\mu\mathbf{H}$$
$$\nabla \times \mathbf{H} = j\omega\mu\mathbf{E}$$
$$\nabla \cdot \mathbf{E} = 0 \tag{3.15}$$
$$\nabla \cdot \mathbf{H} = 0$$

Decomposing *Maxwell's equation* in the guiding direction (z direction) and the transverse directions (x,y directions) and assuming that the medium in which the wave propagates is loss-less, Eq. (3.16) can be described by [9].

$$\nabla_T E_z \times \hat{\mathbf{z}} - j\beta\hat{\mathbf{z}} \times \mathbf{E}_T = -j\omega\mu\mathbf{H}_T$$
$$\nabla_T H_z \times \hat{\mathbf{z}} - j\beta\hat{\mathbf{z}} \times \mathbf{H}_T = j\omega\epsilon\mathbf{E}_T$$
$$\nabla_T \times \mathbf{E}_T + j\omega\mu\hat{\mathbf{z}}H_z = 0$$
$$\nabla_T \times \mathbf{H}_T - j\omega\epsilon\hat{\mathbf{z}}E_z = 0 \tag{3.16}$$
$$\nabla_T \cdot \mathbf{E}_T - j\beta E_z = 0$$
$$\nabla_T \cdot \mathbf{H}_T - j\beta H_z = 0$$

where ∇_T is the differential operator in the tangential plane.
Depending on how the electric and magnetic component varies in the transverse (x,y direction) and the z-direction, different modes can be defined.

$$\begin{cases} E_z = 0, H_z = 0, & \text{\textit{TEM modes}} \\ E_z = 0, H_z \neq 0, & \text{\textit{TE or H modes}} \\ E_z \neq 0, H_z = 0, & \text{\textit{TM or E modes}} \end{cases}$$

The table above depicts TEM, TE and TM modes. TEM modes have electric and magnetic components orthogonal to the propagation direction (z direction). TE modes have no electric component in the propagation direction but the magnetic field is no longer orthogonal to the z direction. TM modes have transverse magnetic component.

3.2.1   TEM Mode

TEM mode waves have no electric $E_z = 0$ or $H_z = 0$ magnetic component in the guiding z-direction and the field components are fully transverse. The magnetic and electric field is determined from Eq. (3.17) and (3.18) respectively [9].

$$\boxed{\mathbf{H}_T = \frac{1}{Z_{TEM}}\hat{\mathbf{z}} \times \mathbf{E}_T} \tag{3.17}$$

where $Z_{TEM} = \sqrt{\frac{\mu}{\epsilon}}$ is the characteristic impedance.

$$\left. \begin{array}{l} \nabla_T \times \mathbf{E}_T = 0 \\ \nabla_T \cdot \mathbf{E}_T = 0 \end{array} \right\} \tag{3.18}$$

Waveguides which support TEM mode propagation have the properties that the *cutoff frequency* $f_c = 0$ or equivalent with the *cutoff wavenumber* $k_c = 0$. The wave impedance of a TEM mode is the same as for a plane wave in a lossless medium [29] and is determined from

$$Z_{TEM} = \frac{|E_T|}{|H_T|} = \frac{\omega\mu}{\beta} = \sqrt{\frac{\mu}{\epsilon}} \tag{3.19}$$

where the wave impedance is a function of the transverse field components and material constants. TEM modes can only propagate in two or higher order conductor system [26].

3.2.2   TE Mode

When $E_z = 0$ and $H_z \neq 0$ the mode is named TE mode. It implies that the mode can have a magnetic component in the propagation direction. Eq. (3.20) determines all the field components for the TE modes.

$$\left. \begin{array}{l} \nabla_T^2 H_z + k_c^2 H_z = 0 \\ \mathbf{H}_T = -\dfrac{j\beta}{k_c^2} \nabla_T H_Z \\ \mathbf{E}_T = Z_{TE} \mathbf{H}_T \times \hat{\mathbf{z}} \end{array} \right\} \tag{3.20}$$

The TE wave impedance is determined from

$$Z_{TE} = \frac{E_x}{H_y} = \frac{-E_y}{H_x} = \frac{\omega\mu}{\beta} \tag{3.21}$$

were β is the index of the mode discussed in the beginning of this chapter. Z_{TE} is frequency dependent and the TE mode can propagate both in a closed conductor as well as in a two or higher order conductor system [26].

3.2.3   TM Mode

Unlike the TE mode the TM mode have $H_z = 0$ and $E_z \neq 0$. To determine the field component for the TM mode the equation (3.22) applies.

$$\left. \begin{array}{l} \nabla_T^2 E_z + k_c^2 E_z = 0 \\ \mathbf{E}_T = -\dfrac{j\beta}{k_c^2} \nabla_T E_Z \\ \mathbf{H}_T = \dfrac{1}{Z_{TM}} \hat{\mathbf{z}} \times \mathbf{E}_T \end{array} \right\} \tag{3.22}$$

The TM wave impedance is determined from

$$Z_{TM} = \frac{E_x}{H_y} = \frac{-E_y}{H_x} = \frac{\beta}{\omega\epsilon} = \frac{\beta z}{k} \qquad (3.23)$$

As for the TE case , Z_{TM} is also frequency dependent, and the TM mode can be triggered in closed conductor as well as in a two or higher order conductor system[26].

3.2.4 Operating Bandwidth

The operating bandwidth varies depending on the kind of waveguide system used. Typically for a TEM waveguide the lowest theoretically possible propagation mode starts at DC which means that the lowest mode has no *cutoff frequency*. It is possible for higher order modes to propagate in waveguides depending on the geometry of the fixture. The upper frequency limit is determined by the *cutoff frequency* of the next higher order mode. If a signal is transmitted, it is important to know which mode is carrying the signal to avoid distortion and dispersion. The operating frequency interval, ω, can be defined as [9]

$$\omega_{c1} < \omega < \omega_{c2} \qquad (3.24)$$

where ω_{c1} is the *cutoff frequency* for the used mode and ω_{c2} is the *cutoff frequency* of the next higher order mode.

TE and TM modes defines the upper limit of the usable bandwidth in a TEM waveguide. TE and TM modes have a lower limit for the *cutoff frequency* which cannot be zero. Coaxial cable is a typical example of a TEM waveguide where the operating bandwidth is defined from DC to the first higher order propagation mode [9]. The operating bandwidth of a transmission line will be discussed further in section 3.5.

3.3   Transmission line

Structures designed to transmit a signal with information or power from point *a* to point *b* are the definition of a transmission line [30]. The transmission line is designed to carry Transverse ElectroMagnetic (TEM) waves in a given direction often denoted the $\pm\hat{z}$ direction, where z is the propagation direction along the structure. Different kinds of transmission lines exists, such as parallel plate waveguides, microstrip lines and coaxial lines which are described below.

3.4   Characteristic impedance

The characteristic impedance of a transmission line is given by Eq. (3.25), which depends on the line geometry and the material of which the wave is propagating [29].

$$Z_0 = \frac{V_0}{I_0} \tag{3.25}$$

where V_0 is the incident voltage and I_0 is the incident current.

3.5   Higher order modes

The *cutoff frequency* is defined as the frequency at which the mode can start to propagate in the transmission line. Undesirable effects can occur if two or more modes with different propagation constants are propagating at the same time. Typically for a transmission waveguide several modes that propagate at the same time affect each other by distortion and dispersion. This causes problem because the actual mode that is carrying the transmitted signal may become unknown.

3.6   Parallel Plate Waveguide

A parallel plate waveguide consists of two parallel plates which are used for low loss transmissions of signals at microwave frequencies. The conducting plates are separated by a distance h, as shown in Fig. 3.1. The gap between the two plates can be filled with a dielectric material with permittivity ϵ and permeability μ_0. The strip width w of the plates is often assumed to be much greater than the separation h. This results in a sufficiently small variation in x which implies that the fringing field outside the waveguide, described more in section 3.6, can be ignored.
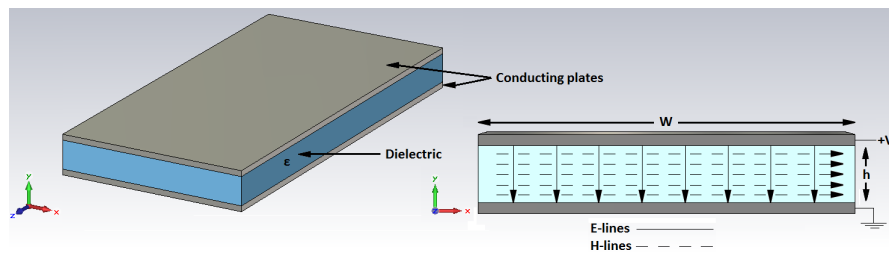
Figure 3.1: E- and H-fields of a parallel Plate transmission line.

The electric and magnetic fields propagate inside the waveguide in y respective x direction. They can be seen as vector components according to the *Helmholtz equation* [29] which is a reduced form of the *Maxwell's equation*.

$$\nabla^2 \mathbf{E} + k^2 \mathbf{E} = 0 \tag{3.26}$$

where the constant $k = \omega \sqrt{\mu \epsilon}$ is defined and called the *wave number*.

3.7   Microstrip line

A microstrip line, as shown in Fig. 3.2a, is a type of planar transmission line where a conductor of width w is printed on a thin, grounded dielectric substrate [31]. The substrate, of thickness h, is placed between the microstrip and ground plane and has the relative permittivity ϵ_r. As can be seen in Fig. 3.2b, because of the sufficiently small width w of the strip compared to the ground plane width, there is a field outside the waveguide called the fringing field that must be taken into account. In this thesis the dielectric is defined as air, which leads to that the microstrip is embedded in air. This constitutes a simple TEM transmission line. For a dielectric with $\epsilon_r > 1$, the microstrip can no longer support a pure TEM wave. The simple explanation is that the phase velocity for the wave is not the same in air as in the dielectric medium, and the wave becomes a quasi-TEM mode [29]. This complicates the calculations and needs more advanced analysis techniques to understand the phenomena.
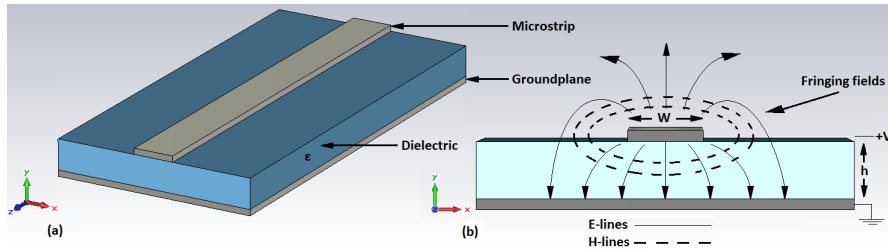
Figure 3.2: E-, H- and fringing fields of a microstrip transmission line.

3.7.1   Characteristic Impedance of a microstrip line

The characteristic impedance can be calculated in several ways. Some of the most accurate one is the *Hammerstad and Jensen's* [32] where Z_0 can be calculated according to Eq. (3.27).

$$Z_0 = \frac{n_0}{2\pi \sqrt{e_{eff}}} \ln \left(\frac{f(u)}{u} + \sqrt{1 + \frac{4}{u^2}} \right) \tag{3.27}$$

where

$$f(u) = 6 + (2\pi - 6) \left(- \left[\frac{30.666}{u} \right]^{0.7528} \right)$$

and

$$u = \frac{w}{h}$$

The effective dielectric constant ϵ_{eff} is calculated by

$$\epsilon_{eff} = \frac{\epsilon_r + 1}{2} + \frac{\epsilon_r - 1}{2}\left(1 + \frac{10}{u}\right)^{-ab} \tag{3.28}$$

where

$$a = 1 + \frac{1}{49}\ln\left[\frac{u^4 + (u/52)^2}{u^4 + 0.432}\right] + \frac{1}{18.7}\ln\left[1 + \left(\frac{u}{18.1}\right)^3\right]$$

and

$$b = 0.564\left(\frac{\epsilon_r - 0.9}{\epsilon_r + 3}\right)^{0.053}$$

Another way to estimate the characteristic impedance [29] is

$$Z_0 = \begin{cases} \frac{60}{\sqrt{\epsilon_e}}ln\left(\frac{8}{u} + \frac{u}{4}\right) & for\ u \leq 1 \\ \frac{120\pi}{\sqrt{\epsilon_{eff}}}\frac{1}{(u + 1.393 + 0.667\ln{(u + 1.444)})} & for\ u \geq 1 \end{cases} \tag{3.29}$$

According to *Kraus* [33], the impedance for a microstrip line can be found as

$$Z_0 = \frac{\eta_0}{\sqrt{\epsilon_r}[u + 2]} \tag{3.30}$$

where η_0 is the wave impedance of free space and ϵ_r the relative permittivity of the dielectric material between the microstrip and ground plane.
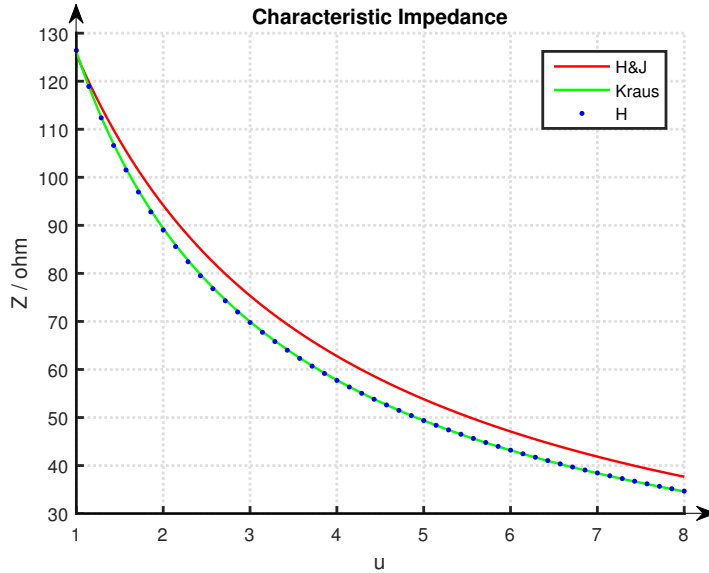As can be seen in Fig. 3.3, the characteristic impedance is plotted for the three equations as a function of u.

Figure 3.3: Characteristic impedance Z_0 of a microstrip line as a function of $u = w/h$ (width/height ratio). Hammerstad and Jensen (red line) from eq. (3.27), Hammerstad (blue dotted line) from Eq. (3.29) and Kraus (green line) from Eq. (3.30).

3.7.2   Higher order modes and operating bandwidth of a microstrip line

For the microstrip line there exist TM and TE modes with higher order modes. The first higher order mode is the TE_{11}, where the *cutoff wavelength* and *cutoff frequency* of the higher order modes [9] can be calculated from Eq. (3.31).

$$\lambda_c = 1.873 \frac{\pi}{2} (a + b)$$
$$f_c = \frac{c}{\lambda_c} = \frac{c_0}{n \lambda_c}$$
(3.31)

Thus, the operating range of the frequency for the TEM mode in a microstrip line is limited to frequencies smaller than f_c, which in turn implies that the operating bandwidth is limited by the geometry of the microstrip.

3.8   Coaxial Line

The coaxial line consists of two concentric conductors of inner and outer radius *a* and *b* respectively, shown in Fig. 3.4, and is the most widely used TEM transmission line. It is designed with a dielectric between the conductors with a dielectric material such as polyethylene or teflon [29].
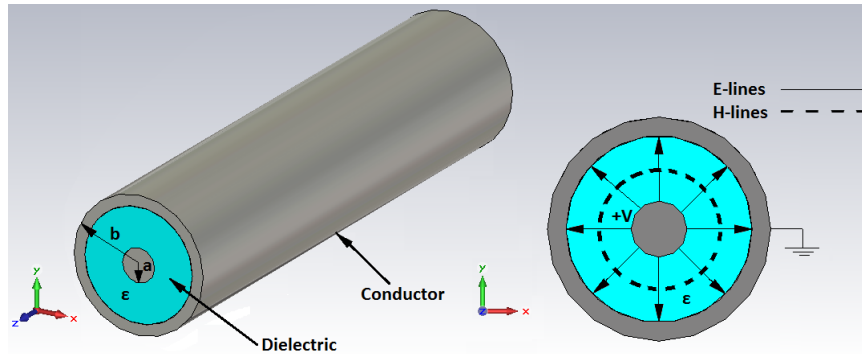
Figure 3.4: E-, H-field of a coaxial transmission line.

The characteristic impedance in a coaxial line [29] can be calculated from

$$Z_0 = \frac{\eta_0}{2\pi} \ln\left(\frac{b}{a}\right) \tag{3.32}$$

where

$$\eta_0 = \sqrt{\frac{\mu_0}{\epsilon_r}} \tag{3.33}$$

3.8.1   Higher order modes and operating bandwidth of a coaxial line

For the coaxial line there can also exist TM and TE modes, where the TE mode is the dominant one. The dimensions of the coaxial cable sets an upper limit of the frequency where TE_{11} mode and higher order modes starts to propagate. This frequency is the *cutoff frequency* for the coaxial cable and sets an upper limit of the operating frequency. The *cutoff frequency* [29] can be calculated from Eq. (3.34).

$$f_c = \frac{ck_c}{2\pi\sqrt{\epsilon_r}} \tag{3.34}$$

where

$$k_c = \frac{2}{a+b} \tag{3.35}$$

3.9   Impedance matching

Impedance matching includes various techniques to maximize the transmitted power or minimize the reflections in a system with electrical signals [30]. For the TEM cell, two transitions from coaxial connector to microstrip line need to be taken into account, and that is when the impedance matching comes into the picture. Impedance matching is also considered when making a transition from

a small microstrip to a larger, which is done with tapering technique. To minimize the reflections in a system, this can be achieved when the load impedance converges to the characteristic impedance. For reflection less matching, the load impedance is equal to the characteristic impedance of the transmission line. These techniques are widely used in this project as there is various physical transitions that need to be taken into account.

3.10 Tapering

There are a lot of ways to change the electromagnetic properties in a waveguide such as the characteristic impedance, for example by tapering a microstrip line. This is a way to match the desired bandwidth to a specific impedance, by using multisection matching transformers. The geometry of a tapered line, as can be seen in Fig. 3.5a, is created by N sections divided over the strip line, Fig. 3.5b. The wideband impedance transformers can typically be realized in three different taper setups. Two of them are used in this project, namely the exponential taper and the Klopfenstein taper. These different types of taper methods can be used to obtain different passband characteristics and are treated in chapter 5 while designing the tapering parts of the TEM cell.
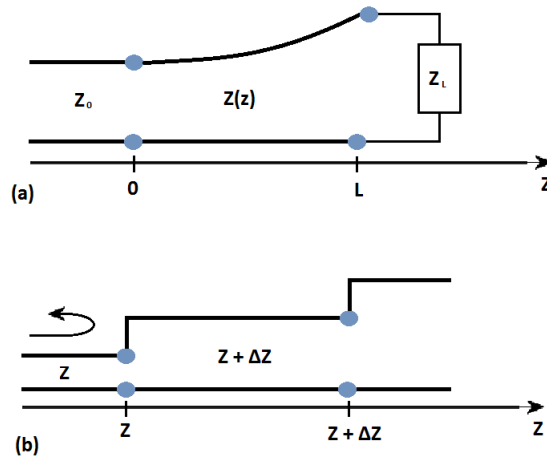
Figure 3.5: Tapering of a transmission line. (a) The tapering and transformation of impedance Z. (b) The tapering step and impedance transform from Z to $Z + \Delta$Z.

The total reflection coefficient at $z = 0$ can be found as

$$\Gamma(\Theta) = \frac{1}{2} \int_{z=0}^{L} e^{-2j\beta z} \frac{d}{dz} \ln\left(\frac{Z}{Z_0}\right) dz \tag{3.36}$$

where $\theta = 2\beta l$. By taking the inversion of Γ, the $Z(z)$ can be found. This is kind of difficult and often avoided. Instead different types of cases are specified where $Z(z)$ is given by an equation [30].

3.10.1 Exponential taper

For an exponential taper, $Z(z)$ is described by

$$Z(z) = Z_0 e^{az} \qquad for \quad 0 < z < L \tag{3.37}$$

To determine the constant a, we begin by calculating $Z(z) = Z(0) = Z_0$. For $z = L$, $Z(L) = Z_L = Z_0 e^{aL}$. This gives a expressed in Z_L and Z_0 as

$$a = \frac{1}{L} \ln \left(\frac{Z_L}{Z_0} \right) \tag{3.38}$$

By using Eq. (3.37) it follows that

$$\begin{aligned} \Gamma &= \frac{1}{2} \int_0^L e^{-2j\beta z} \frac{d}{dz} (\ln e^{az}) dz \\ &= \frac{\ln(Z_L/Z_0)}{2L} \int_0^L e^{-2j\beta z} dz \\ &= \frac{\ln(Z_L/Z_0)}{2} e^{-j\beta L} \frac{\sin \beta L}{\beta L} \end{aligned} \tag{3.39}$$

where β is the propagation constant and L as indicted in Fig. 3.6.

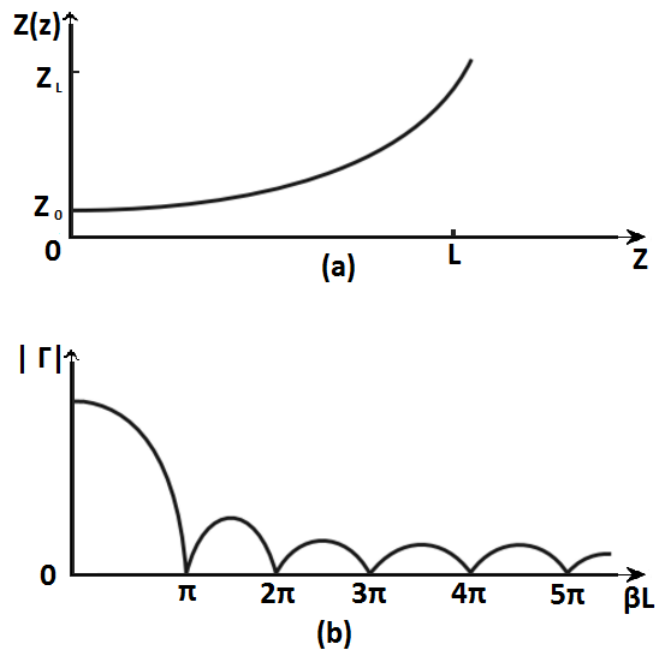**Figure 3.6:** Exponential tapering of a transmission line. (a) The tapering and transformation of impedance. (b) Resulting reflection of a matching section.

3.10.2   Klopfenstein taper

The Klopfenstein taper is a method used in designing connectors, and can also be seen as the optimum tapering method for the microstrip line section of the TEM cell, with respect to low reflection coefficient over the passband for a given tapering length [29, 30, 34]. It is described by a stepped Chebyshev transformer where the number of sections increases to infinity.
The logarithmic characteristic impedance is given by the following equation.

$$\ln Z(z) = \frac{1}{2} Z_0 Z_L + \frac{\Gamma_0}{\cosh A} A^2 \phi \left(\frac{2z}{L} - 1, A \right) \qquad for\, 0 \le z \le L \qquad (3.40)$$

where

$$\phi(x, A) = -\phi(-x, A) = \int_0^x \frac{I_1(A\sqrt{1 - y^2})}{A\sqrt{1 - y^2}} dy \qquad for\, |x| \le 1 \qquad (3.41)$$

which is a defined function of x and A where I_1 is the modified Bessel function. Eq. (3.41) has some special cases with the following values in (3.42).

$$\phi(0, A) = 0$$
$$\phi(x, 0) = \frac{x}{2}$$
$$\phi(1, A) = \frac{\cosh A - 1}{A^2} \qquad (3.42)$$

Besides these special cases, Eq. (3.41) needs to be calculated numerically. The concept is used when designing the tapered sections of the waveguide setup.

Chapter 4

Simulation and measuring tools

4.1 Scattering parameters

The scattering parameters (S-parameters) are a measure of transmitted and reflected amplitude of the signal and describe the electric behavior in a linear two-port network [9]. The S-parameters are essential for a measuring setup such as the TEM cell. A typical TEM cell is characterized as a two-port with circuit parameters as seen in Fig. 4.1, where the incoming waves a_1 and a_2 relate to the outgoing waves b_1 and b_2, respectively. For the respective ports, the transmitted signal are denoted with S_{12}, S_{21} and reflected signal S_{11}, S_{22}.
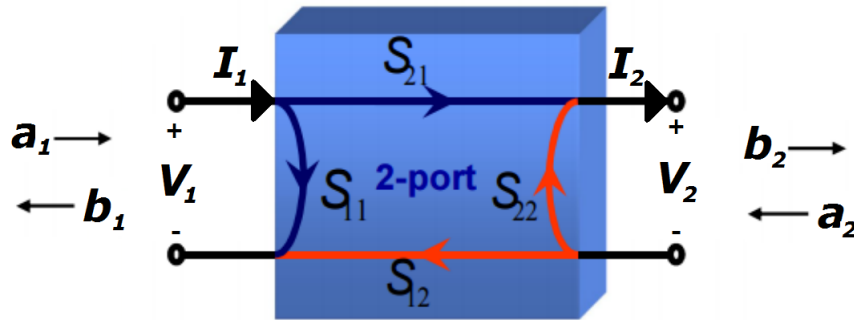

Figure 4.1: Scattering parameters for a two-port, from [45].

The transfer matrix $ABCD$ at port 1 which relates the voltage and current to port 2 is written as [9]:

$$\begin{bmatrix} V_1 \\ I_1 \end{bmatrix} = \begin{bmatrix} A & B \\ C & D \end{bmatrix} \begin{bmatrix} V_2 \\ I_2 \end{bmatrix} \qquad (transfer\ matrix) \qquad (4.1)$$

The impedance and admittance matrix relates the total voltages and currents on the ports, where the impedance matrix is shown in Eq. (4.2). The admittance is calculated by taking the inverse of the impedance matrix.

$$\begin{bmatrix} V_1 \\ V_2 \end{bmatrix} = \begin{bmatrix} Z_{11} & Z_{12} \\ Z_{21} & Z_{22} \end{bmatrix} \begin{bmatrix} I_1 \\ -I_2 \end{bmatrix} \qquad (impedance\ matrix) \qquad (4.2)$$

The transfer and impedance matrices is often denoted T respective Z, where:

$$T = \begin{bmatrix} A & B \\ C & D \end{bmatrix}, \qquad Z = \begin{bmatrix} Z_{11} & Z_{12} \\ Z_{21} & Z_{22} \end{bmatrix} \tag{4.3}$$

The outgoing waves b_1 and b_2 can be calculated by multiplying the incoming wave parameters a_1 and a_2 with the scattering matrix in Eq. (4.4), and thus relates the incoming wave with the outgoing wave.

$$\begin{bmatrix} b_1 \\ b_2 \end{bmatrix} = \begin{bmatrix} S_{11} & S_{12} \\ S_{21} & S_{22} \end{bmatrix} \begin{bmatrix} a_1 \\ a_2 \end{bmatrix}, \qquad S = \begin{bmatrix} S_{11} & S_{12} \\ S_{21} & S_{22} \end{bmatrix} \quad (scattering\ matrix) \tag{4.4}$$

where the traveling wave variables are defined by

$$a_1 = \frac{V_1 + Z_0 I_1}{2\sqrt{Z_0}} \qquad a_2 = \frac{V_2 - Z_0 I_2}{2\sqrt{Z_0}}$$
$$b_1 = \frac{V_1 - Z_0 I_1}{2\sqrt{Z_0}} \qquad b_2 = \frac{V_2 + Z_0 I_2}{2\sqrt{Z_0}} \tag{4.5}$$

4.2   Simulation Procedure

The simulation procedure consist of the two numerical programs CST (Computer simulation technology) and Matlab. CST is a numerical simulation tool which is used to solve Maxwell's equations. It is a cad-based program that has been used in this thesis to draw parallel plate lines, microstrip lines and coaxial waveguides with different dimensions and dielectric materials to simulate the characteristic impedance. Matlab was used as a support while comparing the theory with the simulated results in CST, mainly for numerical calculations of characteristic impedance of microstrip and coaxial cables used in modeling the TEM cell. Further on, Matlab is used to run the Nicolson-Ross Weir and Baker Jarvis algorithm, described in section 2.4, to determine the constitutive variables for different types of material.

Four different designs of coaxial connectors have been developed and simulated to get the best transition for the TEM cell with respect to low reflection and high transmission. To decide which connector that was most suitable for the TEM cell, the E-field patterns and the S-parameters were studied. The program offers simulation in both frequency and time domain to compare the results. Different types of ports, waveguide port, discrete port and lumped element were used to study various types of transmission signals through the system.

The TEM cell was parameterized so that every parameter could be optimized by the CST optimizer that uses the Trust Region Framework algorithm to find the most suitable values. Several simulations were made to optimize it for maximum transmission, minimum reflection and for combinations of the two. The simulated data was exported into Matlab in a Touchstone file to be able to run

the Nicolson-Ross-Weir and Baker Jarvis algorithm. This gave some interesting results of how the transmission and reflection parameters affect the resulting simulated electromagnetic variables of different types of material, which is evaluated in chapter 5.

4.3   Measurements

The ASTM standards is a collection of international technical standards for materials, products and systems, just to name a few. The publishing work and developments is voluntarily produced for the public. ASTM international [12, 35] has a standard test method for measuring relative complex permittivity and permeability for different kind of waveguide structures which is of value in this thesis. Setups and procedures must be the same for each measurement to achieve credible results.

4.3.1   Network Analyzer

A network analyzer is an instrument that can be used when analyzing an electrical circuit. When working at higher frequency, voltage and current do not serve as a reliable measure. To perform accurate measurement at higher frequency reflection and transmission are used. The VNA (vector network analyzer) measures the S-parameters which give information about amplitude and phase. For this thesis the VNA is used for two-port measuring because the TEM cell can be electrically seen as a two-port. Calibration is performed to handle the phase velocity variations of the excited wave. The calibration is necessary because one needs to change the reference plane to the test samples surface and to eliminate signals which are not generated by the test sample. Length of the cable and the transition between the different connectors contributes to the losses.

4.3.2   Extracting the complex permittivity and permeability

To calculate the constitutive parameters a Touchstone file or a s2p file is created from the network analyzer. The files are loaded in Matlab using a script which then processes the loaded data using the algorithms and plots the result. The plots depict the real part of the complex permittivity and the imaginary part of the complex permittivity. The real part of the complex permittivity gives the relative permittivity of the test sample while the imaginary part displays the electric loss of the test sample.

Chapter 5

Design

Considering the requirements for the measurement setup and the theory from chapter 1-4, a number of decisions were made for the final design. The decisions made for the design procedure are motivated and substantiated with the information given in the theory part and the specification of the design given in the list below.

- Frequency range 0-5GHz

- TEM waveguide fixture

- Easy setup for test sample compared to other existing solutions

- 2-port system with input impedance to match 50Ω

The design specification requires that the waveguide is a two-conductor system which support TEM waves. TEM waves support the required $f_c = 0$ which means that the lowest propagation mode in the fixture is defined from 0Hz.
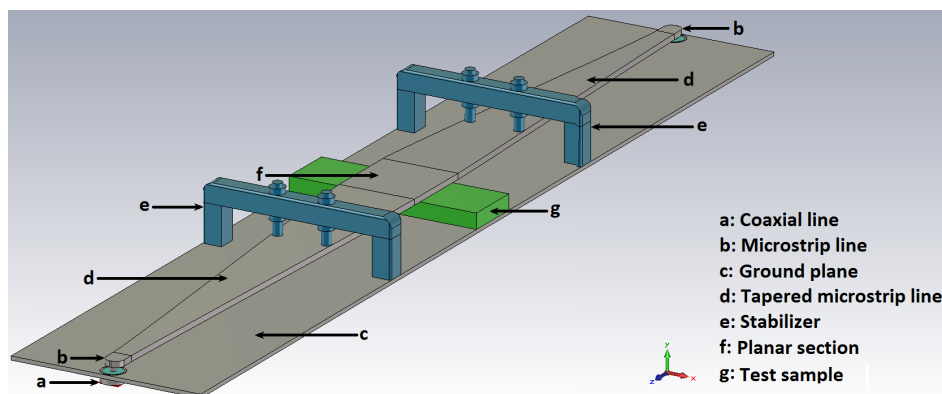

a: Coaxial line
b: Microstrip line
c: Ground plane
d: Tapered microstrip line
e: Stabilizer
f: Planar section
g: Test sample

Figure 5.1: Final design with inserted test sample.

The difficult part of the design decision is the fact that the equations for the microstrip waveguide is assumed to have a dielectric material between the ground plane and the conductor. The formula defined for the microstrip impedance, Eq.

(3.27) yields for material of permittivity higher than $\epsilon_r = 2$. For this project air is used as dielectric material between the two conducting plates where the permittivity is $\epsilon_r = 1$. The formulas are approximately defined, and the inaccuracy of the formulas for permittivity $\epsilon_r = 1$ needs to be taken into account. The fixture requires a 2-port setup for transmitting and receiving the signal. The final design is shown in Fig. 5.1 and 5.2. The different design approaches will be discussed in the following sections where the motivation and conclusion are presented.
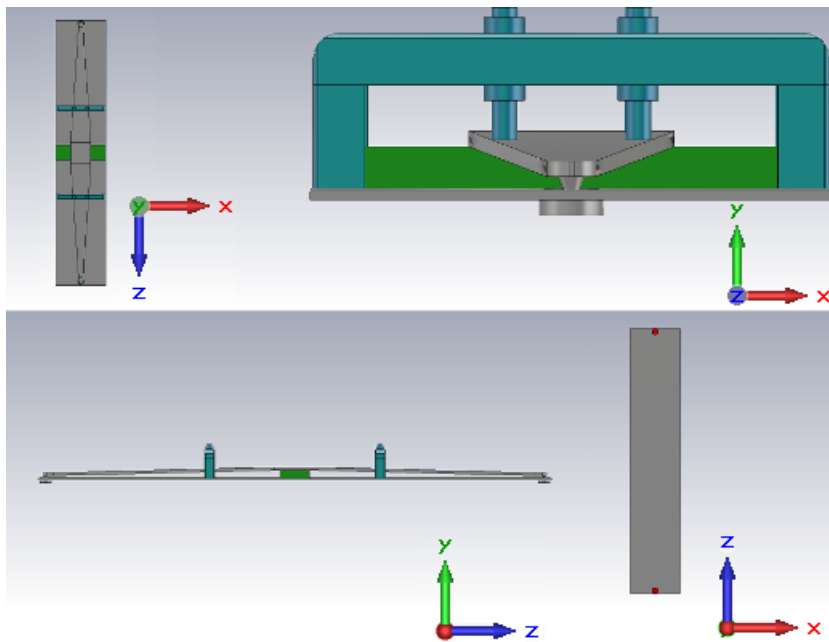

Figure 5.2: Final design with inserted test sample, where the excitation of the electromagnetic wave is pointing in the Z-direction. The two coaxial ports from underneath can be seen in the lower picture to the right.

5.1   Microstrip line

The first part of the waveguide is to construct a microstrip line, as can be seen in the highlighted part in Fig. 5.3, with vacuum as the defined dielectric material with permittivity $\epsilon_r = 1$. Microstrip lines are planar transmission lines which have analogies with the coaxial transmission lines. Both are two-conductor system but with the difference that the coaxial line is a closed system and is not being affected by the surrounding environment.
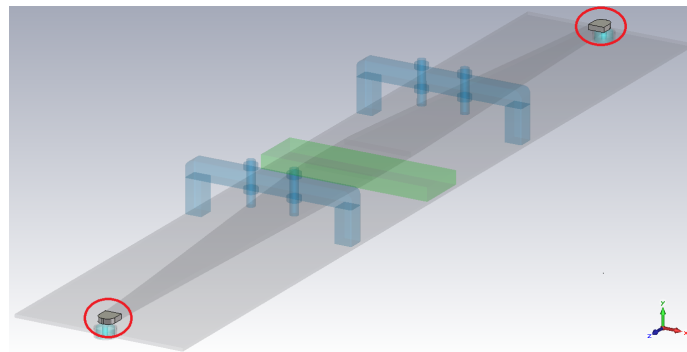
Figure 5.3: Microstrip line with bent edges in highlighted shape.

The microstrip line is matched to 50Ω where the width to height ratio is fundamental for the matching. Eq. (3.27) gives an approximate value of the characteristic impedance of the microstrip. By numerical simulation, a first approximation of a thin microstrip is calculated. Fig. 5.4 shows a simplified model with permittivity $\epsilon_r = 1$ and waveguide ports to analyze how the impedance varies depending on different width to height ratio. The operating bandwidth is set by the *cutoff frequency* for the higher order mode which propagates from around 13GHz. This was determined from Eq. (3.31). The planar section of the TEM cell, which is also a kind of microstrip line, is treated and evaluated in section 5.5.
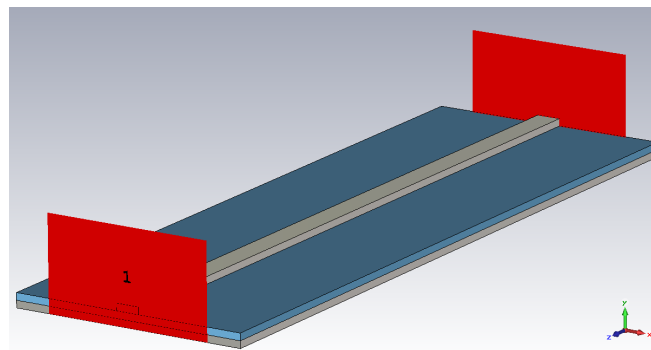

Figure 5.4: Microstrip line with waveguide ports in CST.

The E-field pattern of a microstrip line is shown in Fig. 5.5. The direction of the E-field points towards the ground plane, but the E-field pattern is not perfect. On the sides of the conducting structure there are E-field curves called *fringing fields*. The fringing field is treated later in this chapter. When the excitation platform is designed, the coaxial port needs to be investigated which follows in section 5.2.
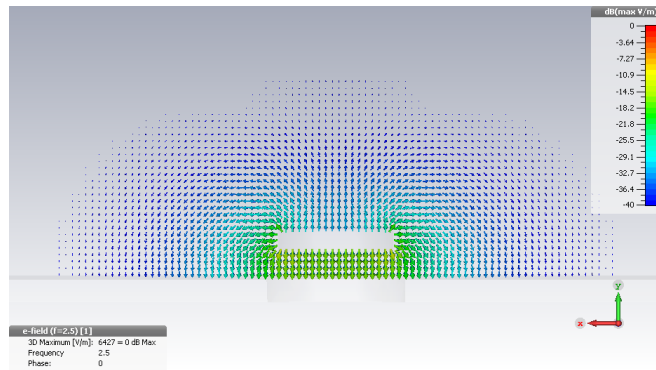
Figure 5.5: Simulated E-field in dB scale of a microstrip line.
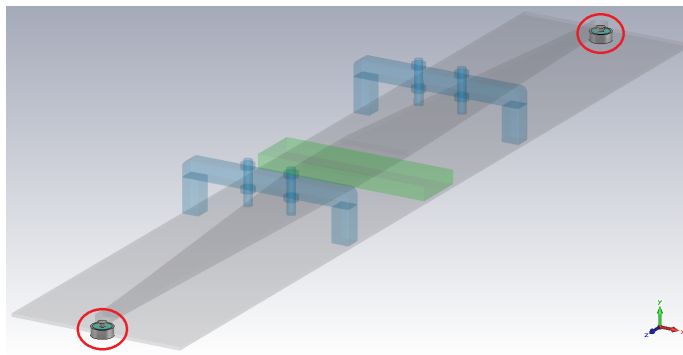
5.2   Coaxial line

Figure 5.6: Coaxial line in highlighted shape.

Coaxial lines are used for the connection between the network analyzer and the waveguide structure as shown in Fig. 5.6. The analytic formula used for the approximation of the characteristic impedance in the coaxial structure is given in Eq. (3.32). The medium used in coaxial connectors is exclusively teflon. The electric wave travels in the z-direction in the dielectric medium of the coaxial structure and the E-field pattern is shown in Fig. 5.7. The E-field is pointed outward from the conducting center pin to the outward ground which capsules the center pin.
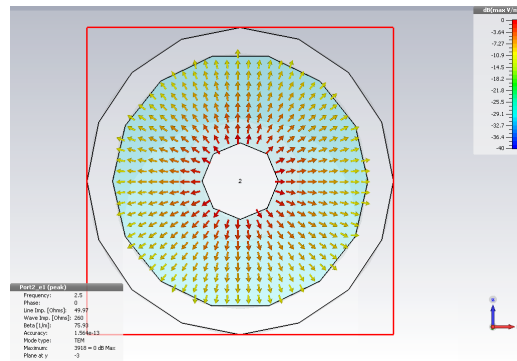
Figure 5.7: Simulated E-field in dB scale of coaxial line.

An important aspect for the decision of what kind of coaxial connector to be used is that the coaxial connector need to be mechanical stable. The specific N-connector works in the frequency range 0-11GHz and has a stable structure with a thick center pin [28]. The *cutoff frequency* for the connector can be calculated from Eq. (3.34) to determine when the next mode can start to propagate in the line and thus determine the operating bandwidth for the connector.

5.3   Transition Coaxial to Microstrip transmission line

Comparing the two E-field patterns of a microstrip and coaxial line in Fig. 5.5 and Fig. 5.7 respectively, it is obvious that the E-field pattern changes, and a transition between the different waveguide structure is difficult. A transition between the two different waveguide fixtures will include discontinuities and in turn cause unwanted reflections [31]. Therefore several transition techniques were investigated to get as smooth transition as possible to the microstrip line. Four of them are further evaluated and discussed below.
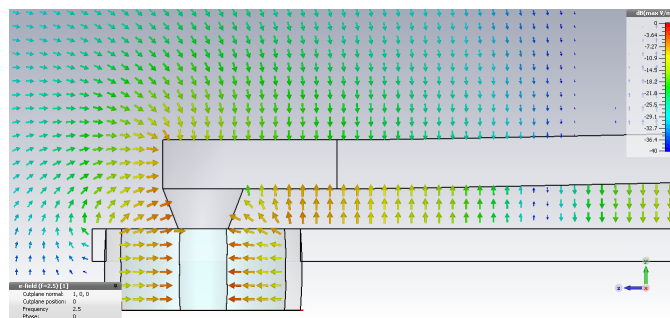

Figure 5.8: Simulated E-field in dB scale of transition from coaxial line to microstrip line.

The transition is investigated and simulated and the result is shown in Fig. 5.8. It can be seen from the figure how the E-field varies from the coaxial line to the microstrip line. The coaxial line contains teflon and the microstrip contains air in the guiding direction. The coaxial part is tapered to smooth the transition and to compensate for the discontinuities and reflections. Referring to section 4.1 and identifying the correct scattering parameter, which for this case is the reflection parameter S_{11}, is a measure of how well matched the transitions can be made. Different setups were simulated by numerically determination which kind of transition will offer the best solution that matches the specification. The *Eisenhart* connector and the reasoning around the mentioned connector [36] together with transition techniques from [37, 38] are used as a source of inspiration while designing the connector with respect to smooth transition with low reflection. The technique used is a tapered part in the connector to get a smooth transition for the E-field while designing a connector from underneath. Fig. 5.9 shows four different kinds of connectors. The reflection and transmission parameter are plotted in Fig. 5.10 and Fig. 5.11. Fig. 5.10 shows the reflection parameter for four different types of coaxial to microstrip connectors.The complexity of the matching is increasing because of the operating bandwidth requirement given in the specifications.
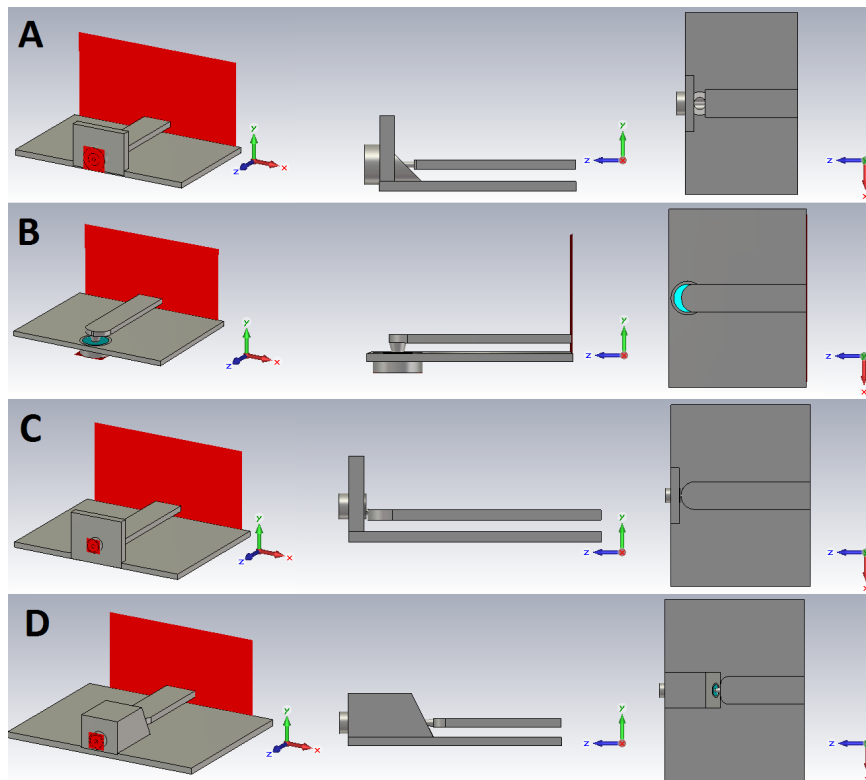

Figure 5.9: Design of Coaxial connectors A-D.

The connector designs in A and D are designed with an outer conductor which is cut with an angle. This is a technique to turn down the E-field against the ground plane of the microstrip. The connector in B is based on ideas on a tapered design from [13], where it is connected from below. This makes the E-field vary in a way that makes the transition smoother. From the theory in section 3.10, the tapered design does match the microstrip to a desirable impedance. The connector C is based on the *Eisenhart* connector as mentioned above, which has a type of tapered inner conductor where it is also turned down against the microstrip. The theory of the Klopfenstein method is also described in section 3.10.2.
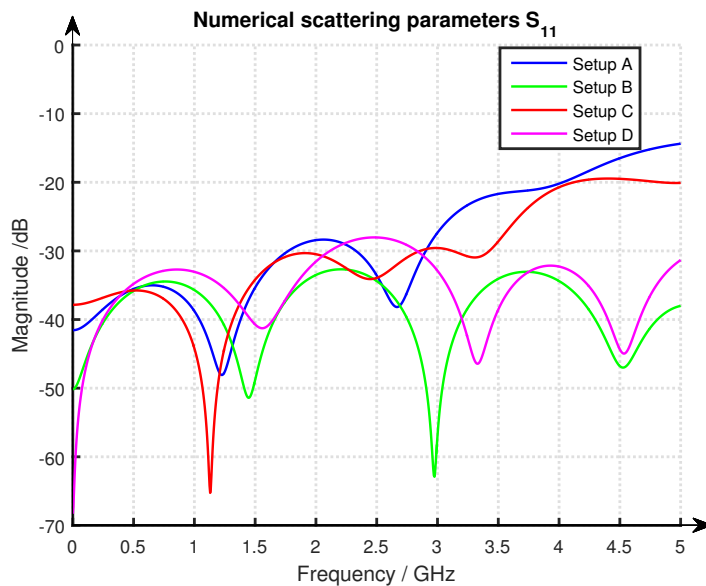

Figure 5.10: Simulated reflection coefficient S_{11} for the different coaxial connectors.
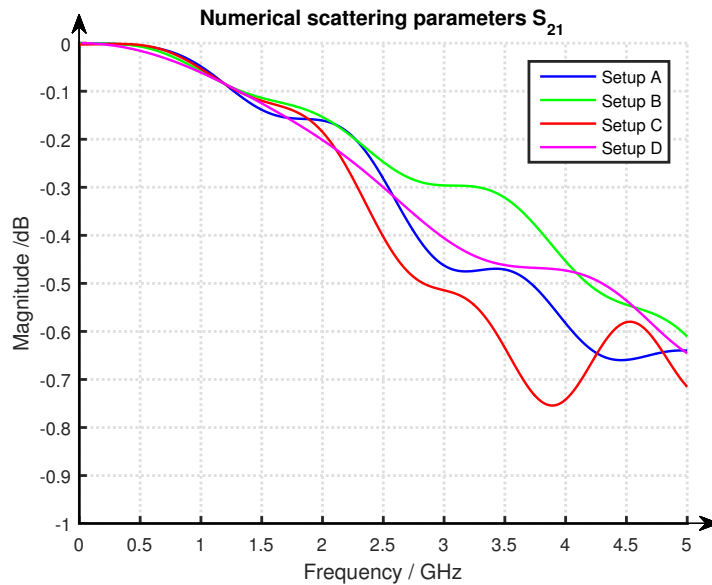
Figure 5.11: Simulated transmission coefficient S_{21} for the different coaxial connectors.

By examining the scattering parameters further, one can see that both the reflection S_{11} and transmission parameters, S_{21} in Fig. 5.10 and Fig. 5.11 respectively, have a slight correlation. For example the green line (setup B) have the best transmission parameters because it's reflection parameters is the lowest over the measured frequency range. The important part is to examine how the two different parameters affect the calculation of the electric permittivity and permeability. This is done by multiple simulations with a given material which for this case is teflon. Because of the complexity of the problem one needs to vary a number of variables and compare the result relative to the expected output. Connector in B offers low reflection over the whole spectrum and has the best transmission, thus this connector is chosen to be manufactured for the TEM cell.

5.4   Tapered microstrip lines

The excitation platform is matched to the coaxial cable and its dimension is thereby limited by the coaxial cable. Referring to the design specification of the waveguide, sample that are of manageable size concerning manufacturing of different kind of test material is the main aspect. This requires a transition from the small microstrip to a larger microstrip, inspired from Klopfenstein which is discussed in section 3.10.2. The microstrip was simulated in CST and dimensions of the microstrip was based on ideas from [39, 40], where an optimum tapered transmission line is analyzed. Ideas were also taken from [34], where an improved design with Klopfenstein tapering was investigated. Every little section of the tapering can be seen as a small microstrip. It is important to preserve the matching

and minimize the losses when the tapering is designed. Smooth transitions are important to minimize the risk of triggering higher order modes from propagating in the waveguide and interference with the desired TEM mode.
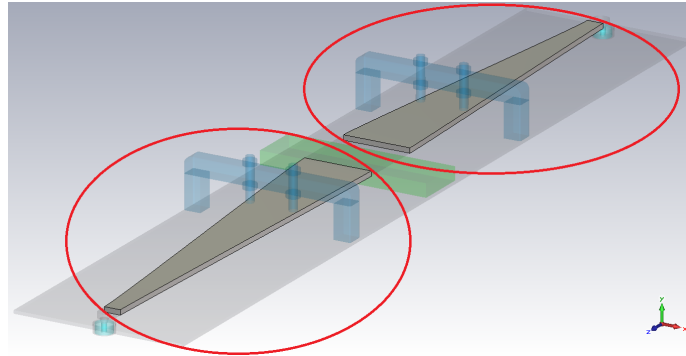

Figure 5.12: Tapered microstrip lines in highlighted shape.

5.5   Planar section of the TEM cell

The planar section shown in Fig. 5.13 can be seen as a larger microstrip, referring to the microstrip line in section 5.1, where the impedance is matched to 50Ω. The size of the planar section is determined from the size of the test sample and the scattering parameters, and is limited of when the higher order modes can start to propagate. According to Eq. (3.31) the first higher order mode can start to propagate at around 2.6Ghz. This mode may start to propagate later as it is affected by the physical geometry of the TEM cell, for example by the tapered microstrip lines and the refined surface to eliminate discontinuities in the material. This counteract the higher order modes to be triggered. The simulation of the structure in CST and then optimizing it for the best matching to satisfy the calculation of the material parameters is the most important aspect when preventing this.
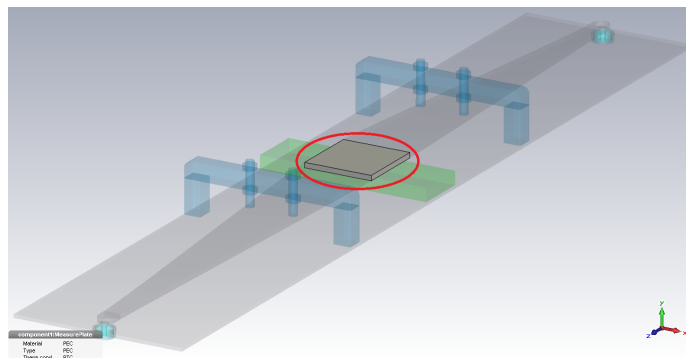

Figure 5.13: The planar section, in highlighted shape, covering the test sample.
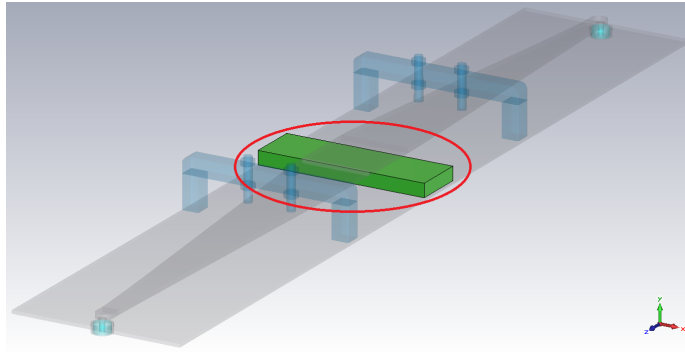
5.6   Test sample

Figure 5.14: The test sample in highlighted shape.

The test sample is placed in between the ground plane and the planar section as can be seen in Fig. 5.14. When the first version of the waveguide fixture is designed, an attempt is made to characterize the material parameters of teflon in the CST simulation environment. Teflon is known to be a stable material with permittivity $\epsilon = 2.1$ for a wide range of frequencies and it serves as a good first experimental test. The Baker Jarvis and Nicolson-Ross-Weir algorithm from section 2.4 is modified to match the given fixture and the permittivity and permeability is calculated from the scattering parameters. To calculate the permittivity in the Baker Jarvis algorithm, a calibration with the empty line is done and the field pattern is shown in Fig. 5.15.
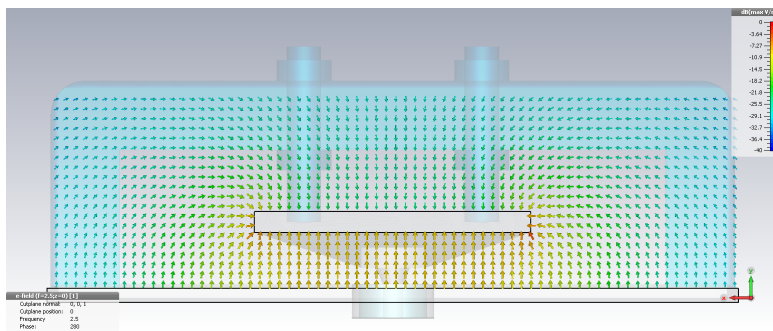

Figure 5.15: Simulated E-field in dB scale of the TEM cell without the test sample.

The E-field is bound to the fixture under the conducting plate and there is also fringing fields. The fringing fields depend on the medium where the electromagnetic waves are propagating. Higher permittivity of the surrounding dielectric material binds the field which in turn result in less fringing fields [31]. To normalize the scattering parameter, an empty line was simulated and then simulation is

done to the actual test piece in the waveguide. The normalization or calibration is done when dividing the two scattering parameters to eliminate losses which does not occur from the actual test sample. Different widths are simulated, while the thickness and height is the same, to analyze how the E-field varies.
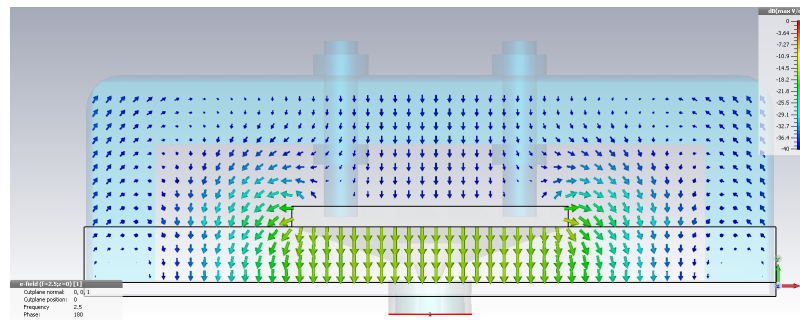

Figure 5.16: Simulated E-field in dB scale with Teflon as test sample. Width of test sample 150mm.

Fig. 5.16 shows the E-fields for a test sample which cover the whole conducting plane and the size of the ground plane. The experiment is made to measure how different widths affect the final value of the calculated permittivity and to study the phenomena of fringing fields and leakage.
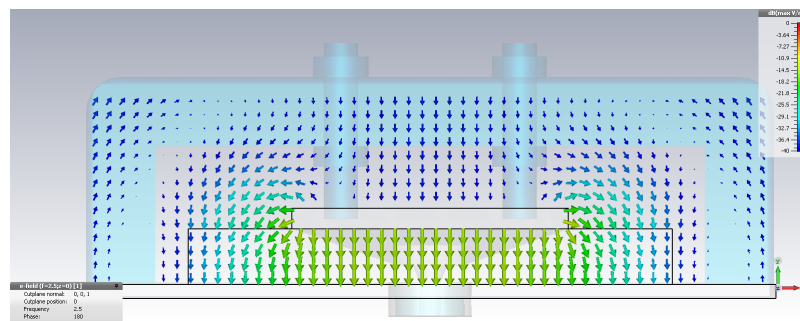

Figure 5.17: Simulated E-field in dB scale of Teflon as test sample. Width of test sample 100mm.
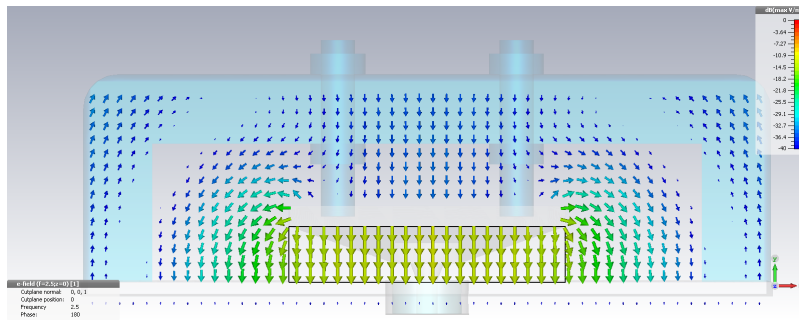
Figure 5.18: Simulated E-field in dB scale of Teflon as test sample. Width of test sample 56mm.

Fig. 5.17 and Fig. 5.18 show simulated E-fields of different widths of the test sample. The E-field pattern does not reveal the whole truth. There is a difference in the electric field distribution due to the different widths but a graph with the different calculated parameters reveals how the result is affected and which width is preferred when doing the measurement. Fig. 5.19 shows the four different cases investigated.

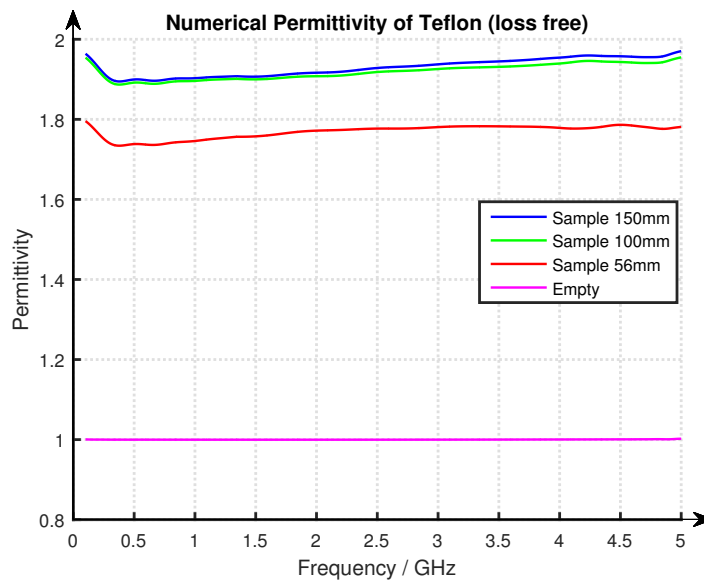
Figure 5.19: Simulated Permittivity for teflon as test sample for different widths.

Referring to Fig 5.19 there is a significant difference between the size and the permittivity. Ideal permittivity for the simulated air is $\epsilon_r = 1$. The smallest test sample has a bigger error due to the leakage of the E-field. To minimize the error, the test sample with width of $150mm$ is chosen.
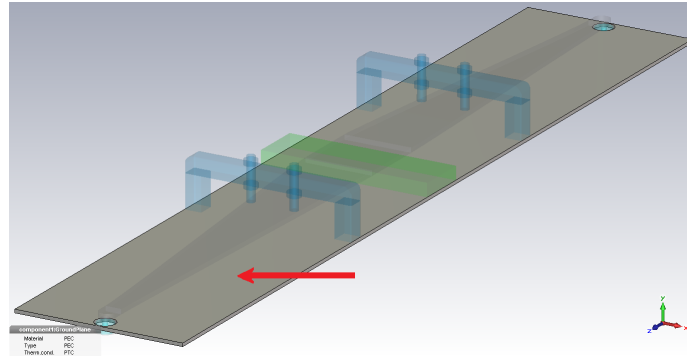
5.7   Ground plane

Figure 5.20: Ground plane of the fixture in highlighted shape.

The size of the ground plane affect both the transmission and the reflection parameter. Different widths of the ground plane was simulated in CST and the scattering parameters was studied. The ground plane is selected to be as small as possible without interfering with the measurement accuracy.

5.8   Stabilizer
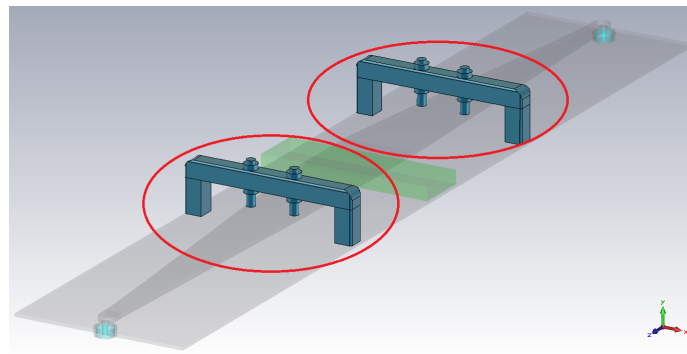
Figure 5.21: Plastic frame with bolts to stabilize and adjust the fixture, in highlighted shape.

The choice to use a plastic frame supporting structure shown in Fig. 5.21 is because of the fixture length and to be able to tighten the test sample so no leakage occurs between the planar section and the ground plane. Another reason is to be able to adjust the width to height ratio matching when connected to the network analyzer. The bolts are mounted to the top of the tapered microstrip and can easily be adjusted by the screws. The stabilizing frame which includes the bolts is

constructed in Delrin (Acetal Resin) which is an electrically insulating and rigid material. The choice of location and dimension of the stabilizer is to make sure that the influence to the E-field is as low as possible.
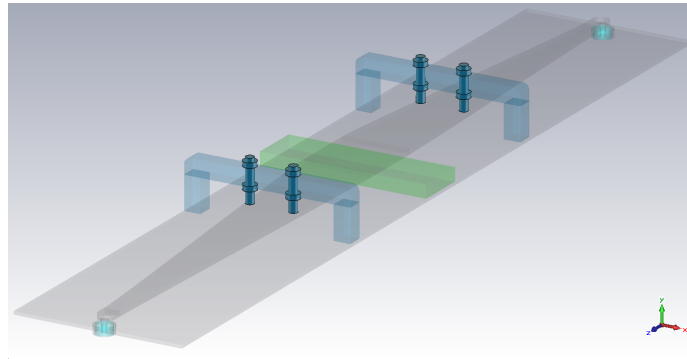

Figure 5.22: Bolts mounted on top of the structure to adjust the width to height ratio.

5.9   Final Simulated Design

Waveguides can be designed in many ways and a number of variables need to be taken into account. When a first layout is designed and the desired result is achieved the waveguide needs to be tested. A table with different data for simulated structures are shown in Fig 5.1.

Table 5.1: Table of dimensions (in mm) of the different setups A-D.

	Setup A	Setup B	Setup C	Setup D
Ground plane	500x150x6	500x150x6	533x150x6	596x150x6
Planar section	40.5x27x3	56x32.2x3	40.5x40x3	45x30x3
Test sample	100x29x9	100x32.2x12	100x30x8	100x30x10

The scattering parameters are simulated in CST. Fig. 5.23 shows the different reflection parameters of the different setups.
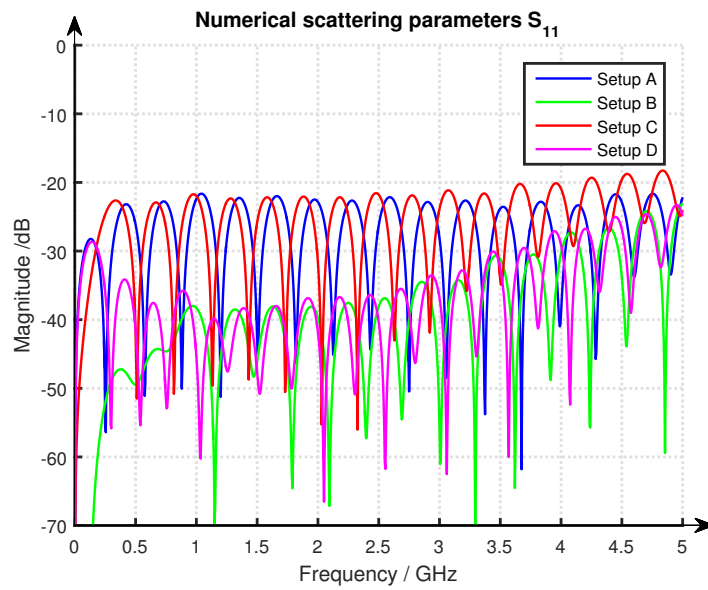
Figure 5.23: Simulated reflection coefficient S_{11} the different setups.

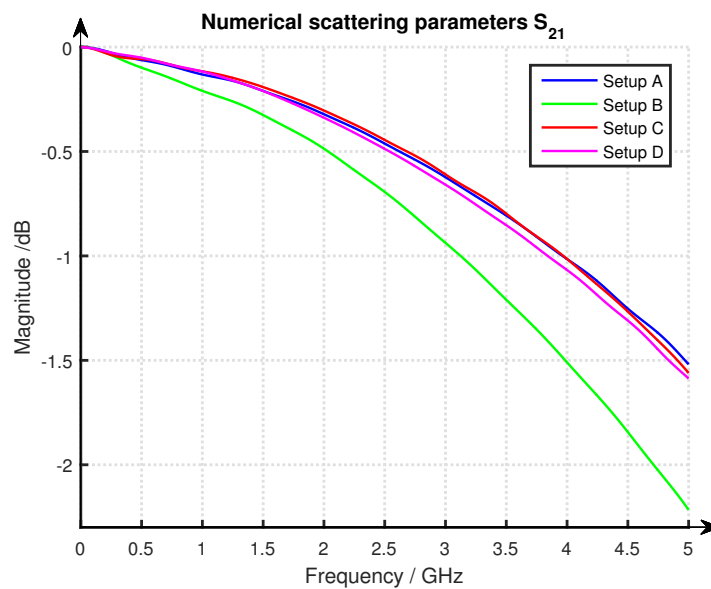Fig. 5.24 shows the transmission coefficients for the setups in the table.

Figure 5.24: Simulated transmission coefficient S_{21} of the different setups.

Having the data plotted one can compare the different setups with each other,

but to achieve relevant results, different materials needs to be measured in the different setups to determine which parameters are most significant for the final design. By setting up a numerical experiment in CST and exporting the scattering parameters, the permittivity and permeability can be determined from the Nicolson-Ross-Weir Eq. (2.11) and Baker Jarvis Eq. (2.13) algorithm. In the following figures there are a range of simulated materials in the different setups. The size and shape of the test sample are the same for all materials, it is only the type of material and setup that varies. The test is performed in such a way that a decision on which design is most appropriate for the task can be selected.
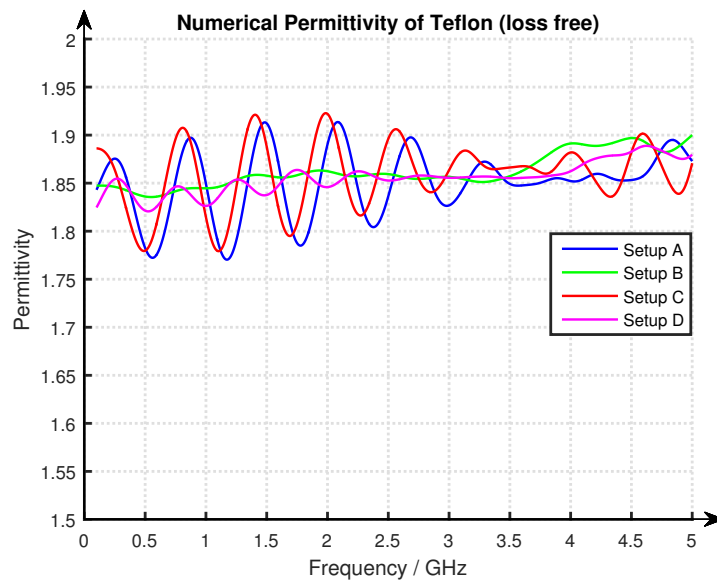

Figure 5.25: Permittivity of Teflon with Baker Jarvis algorithm of the different setups using simulated data.
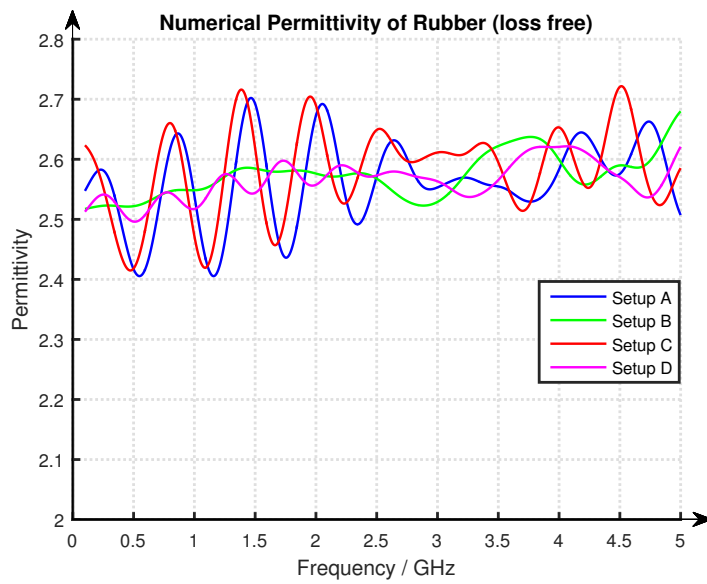
Figure 5.26: Permittivity of Rubber with Baker Jarvis algorithm of the different setups using simulated data.
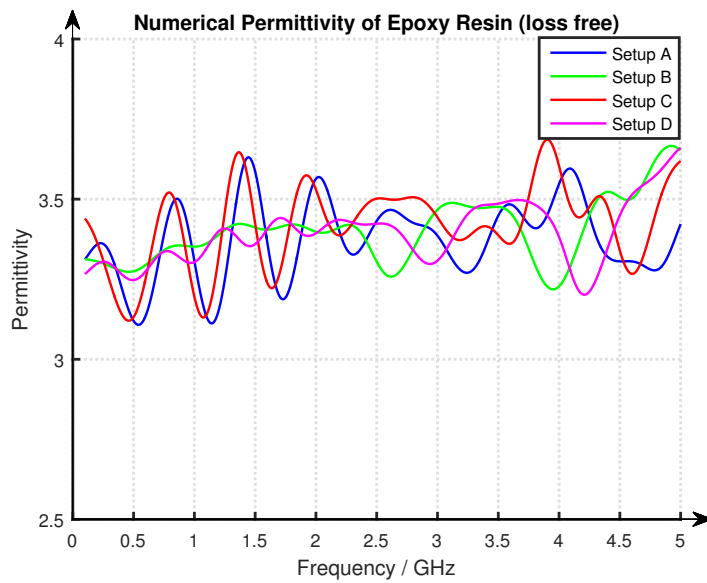
Figure 5.27: Permittivity of Epoxy Resin with Baker Jarvis algorithm of the different setups using simulated data.
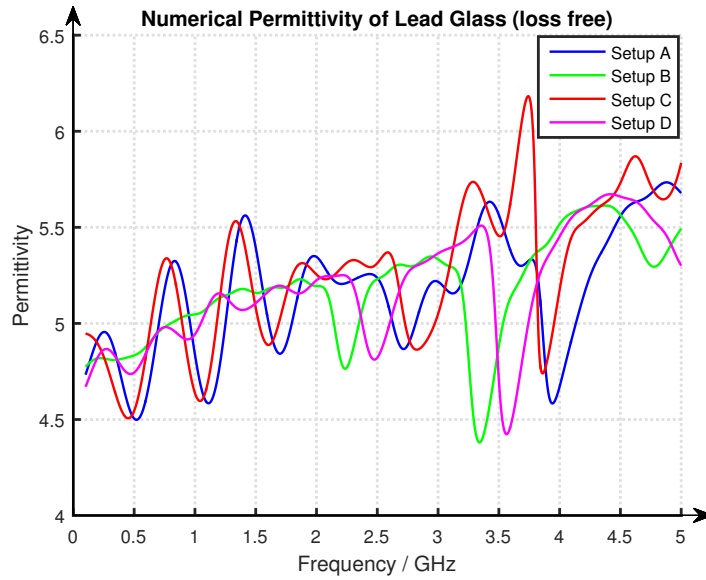
Figure 5.28: Permittivity of Lead glass with Baker Jarvis algo-
rithm of the different setups using simulated data.

Comparing the results in the above Fig. 5.25-5.28 with the simulated permittiv-
ity for different kinds of materials one can predict which setup is best for this
purpose based on the given specification. The setup in B offers smoother plots
of the measured permittivity and has the lowest S_{11} parameter over the spec-
trum, shown in Fig. 5.23. As can be seen in Fig. 5.24, this offers a slightly lower
transmission coefficient S_{21}. To maximize the accuracy of the relevant result the
waveguide with the best reflection parameter, setup B is chosen to be manufac-
tured.
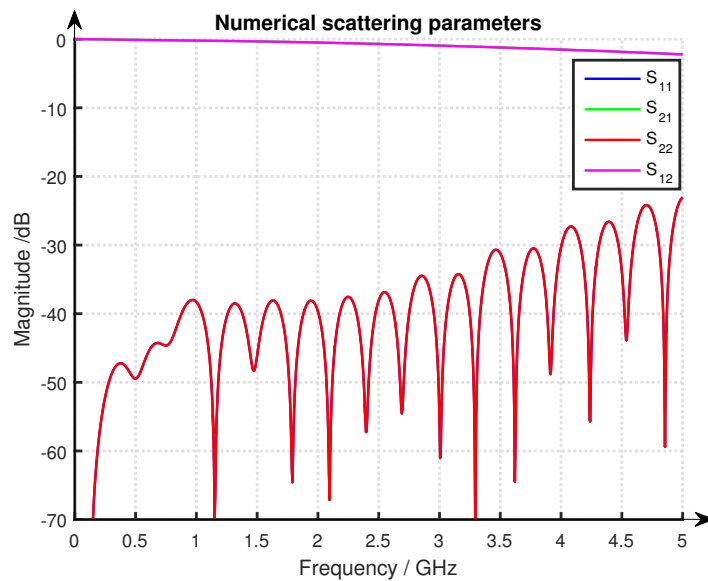
Figure 5.29: Simulated transmission and reflection of the final design (Setup B).

Fig 5.29 shows the scattering parameters for the chosen setup. One can see how the reflection coefficient S_{11} varies over the simulated frequency range. The S_{21} parameter shows the transmission coefficient. The result of the numerical simulation satisfies the expectations on an open waveguide considering interference from ambient and leakage due to the advanced design.

Chapter 6

Manufacturing

6.1 Initial test design

Before manufacturing the actual measuring setup, a test design was made on a microstrip to get an idea of the stability of the material. The transition from an SMA-connector that was soldered onto it was investigated and verification of the theoretically calculated characteristic impedance was made. Brass was used as material for the test setup and was manufactured at Saab. The SMA-connectors were mounted from underneath the ground plane, where the inner conductor of the connector was soldered to the microstrip, as shown in Fig. 6.1. The resulting values showed good transmission and reflections of -20dB over the frequency 0-5GHz while using the network analyzer. By tilting the microstrip, this gave an idea of how much impact the width to height ratio has for the microstrip in sense of the characteristic impedance, as described in section 3.4.

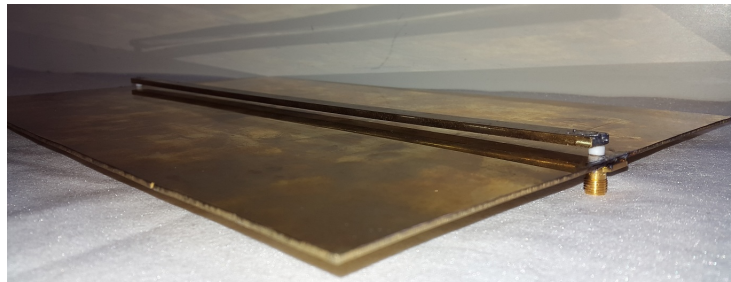**Figure 6.1:** Manufactured test design with coaxial SMA-connectors.

6.2 Materials

The material selected for the measurement setup is aluminum because of its high electrical conductivity and rigid properties. The measurement setup needs to be perfectly matched to the model in CST with respect to straight conducting plates and refined surfaces, to avoid discontinuities in the electromagnetic field. The

measuring setup must also be mechanically stable to handle movements while using or moving the setup. This is mostly managed by the stabilizer that is also used to adjust the setup, as mentioned in section 5.8. The stabilizer frame including bolts is manufactured in Delrin (Acetal Resin), which is a good isolating and rigid material, as described in section 5.8.

6.3   Connector

Figure 6.2: Standard female N-connector.

The coaxial connector is a standard female N-connector, Fig. 6.2, that is mounted from the bottom of the ground plane. It is a large size connector and was chosen instead of the SMA-connector, that was first used on the test design, because of its more rigid structure with a larger inner conductor. The inner conductor of the connector is connected to the microstrip with a cone-shaped structure. The cone-shaped part is first mounted to the connector by "conducting glue", which creates a good electromagnetic transition between the two parts. The connector is then permanently threaded into the microstrip which creates a mechanical stable and highly conducting transition, shown in Fig. 6.3.
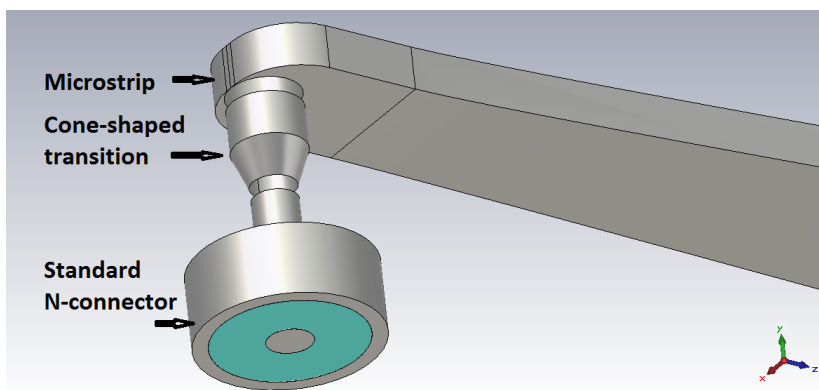

Figure 6.3: Manufactured pieces for the transition between the coaxial connector and microstrip.

6.4   Test sample

The test samples used for the measurements in this project are manufactured in teflon, bakelite and an unknown material and are of size $150x32x12$mm^3. The manufacturing of accurate test sample sample can be a complicated task. The milling machine was used to manufacture the test sample, since the measurement is influenced by how accurate the sample can be made. In this case, the surface smoothness is significant and must be essentially perfect to prevent field leakage as described in section 5.6. The teflon material was the most difficult part to process. It is a soft material that would melt if milled to fast. Therefore the material was processed with the milling machine at slow pace and crystal oil was used to prevent the material from overheating and meltdown. The same procedure was used for the bakelite and the unknown material to get as good quality test samples as possible. Fig. 6.4 below shows the test samples that were manufactured.
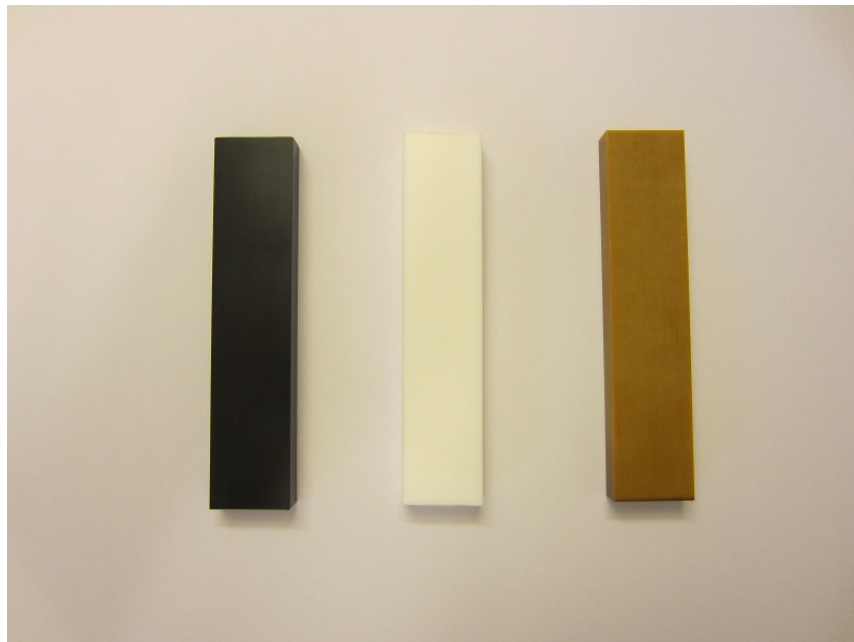

Figure 6.4: Manufactured test samples in an unknown material, teflon material and bakelite material.

6.5   Final design

The measuring setup is manufactured at Saab Aerostructures manufacturing Engineering department. Most of it was made by ourselves with sandpaper, rasp and polisher, with professional assistance while handling the milling machines, Fig. 6.5.

Figure 6.5: Saab Aerostructures manufacturing Engineering Short Series Production and Spares department. A test sample in bakelite is currently being manufactured in the milling machine to the left. The authors are also present in the picture.

The final manufactured design is shown in Figs. 6.6-6.9. The material used is Aluminum as described in section 6.1 and the surface of the structure is processed to get a refined finish. This is done to get rid of any discontinuities in the material to prevent noise and distortion of the signal. The material is first processed with sandpaper, and is then further on processed with a sander. Autosol® Metal Polish was then used to get the glossy refined finish.

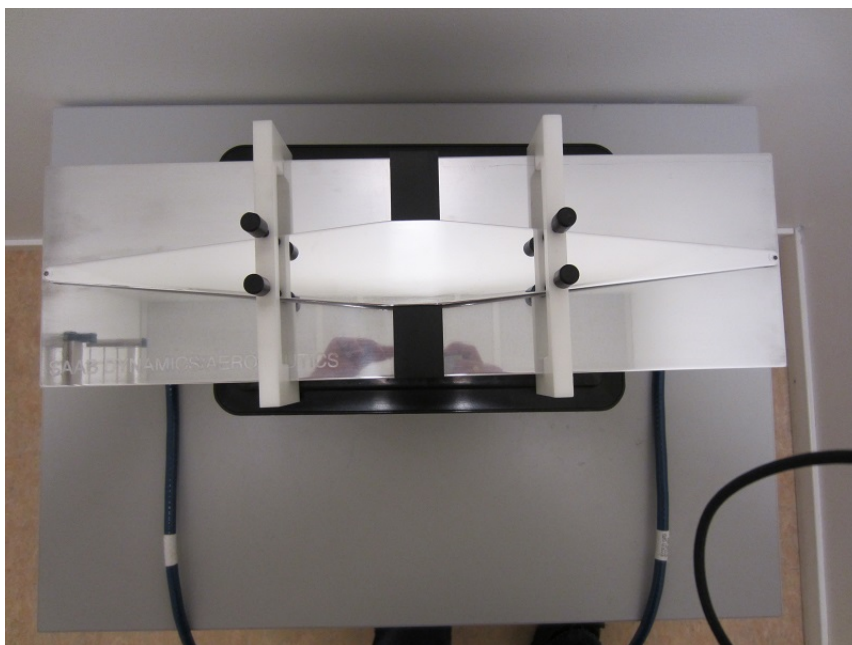**Figure 6.6:** Manufactured final design with an inserted test sample.

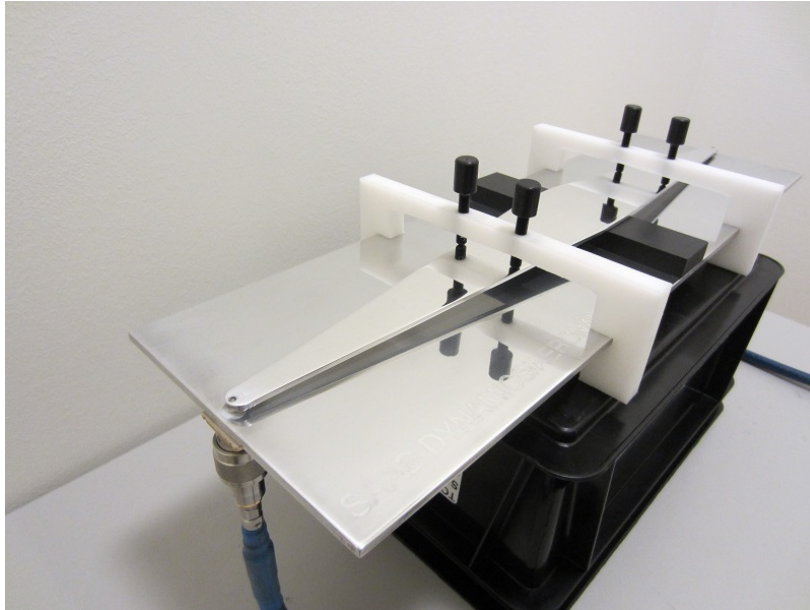**Figure 6.7:** Manufactured final design viewed from above.

Figure 6.8: Manufactured final design viewed from one of the coaxial connectors.

Figure 6.9: Manufactured final design with close up view of the transition from one of the coaxial connectors.

Chapter 7

Validation and Verification

Validation and verification of the manufactured TEM cell is performed using measurements of three different material samples. The three materials are teflon, bakelite and a material with unknown permittivity. Teflon and bakelite are chosen, because of the relatively well-known permittivity over the frequency range 0-5GHz. One important aspect of the material selection is to be able to compare the real measurements with the simulated measurements in the CST environment. By collecting data from the numerical simulations and the actual measurement, different conclusions about the finished prototype can be made. To be able to use the Baker Jarvis Eq. (2.13) algorithm one needs to know the scattering parameters of an empty TEM cell. Scattering parameters are also used to measure how well the TEM cell works and to give a hint of how precise the measurements can be done with the TEM cell. Fig 7.1 shows the scattering parameters for the empty TEM cell.
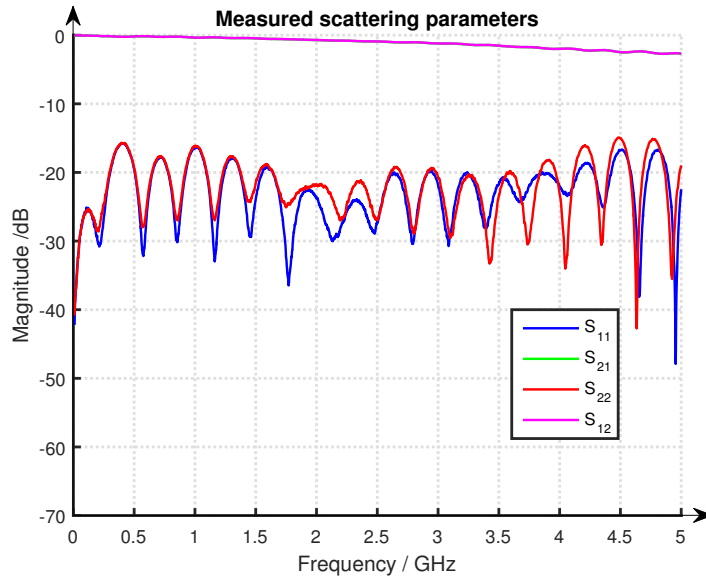
Figure 7.1: Measured scattering parameters of the empty TEM cell.

We also provide the reader with the numerical simulated scattering parameters for the empty TEM cell, in Fig. 7.2, for comparison.
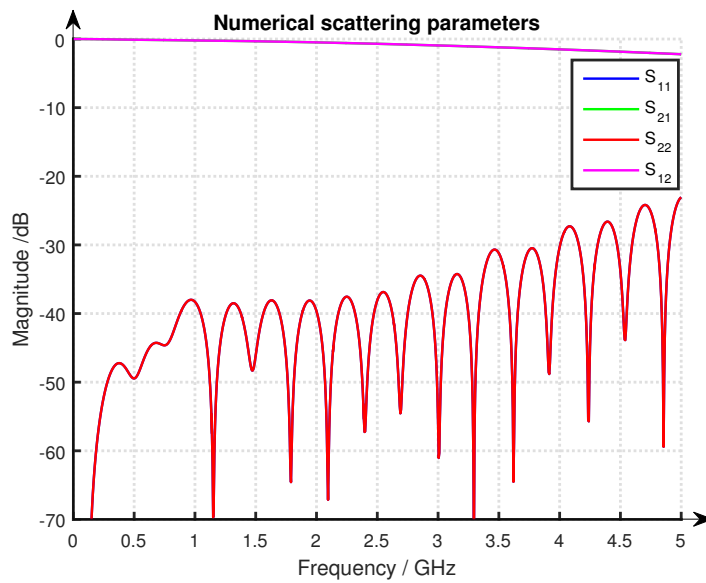

Figure 7.2: Numerical scattering parameters of the empty TEM cell.

Comparing Fig. 7.1 and Fig. 7.2 one can realize that the reflection parameters S_{11} and S_{22} are not the same. The numerical reflection parameters overlap because the two ports are identical with each other which generates the same impedance. For the case with the real setup the ports are hard to manufacture as two identical pairs and some errors may occur from the differences, which is shown in Fig. 7.1. While comparing the measured S_{11} and S_{22}, with the simulated values, one can see that there is a noticeable difference. The simulated values are significant lower over the whole spectrum. This may be because of the fact that the real setup is not perfectly manufactured. There are several transitions which causes discontinuities in the real setup, which in turn affects the reflection coefficient. Transmission coefficient follow each other well. This means that the numerical data is consistent with the measured data.

To verify the results of the TEM cell, a test is done with an empty TEM cell. By knowing that the relative permittivity of air is $\epsilon_r = 1$ and the distance between the two excitation ports is 486mm, one can calculate the permittivity of the empty TEM cell with Baker Jarvis algorithm. The result is shown in Fig. 7.3.
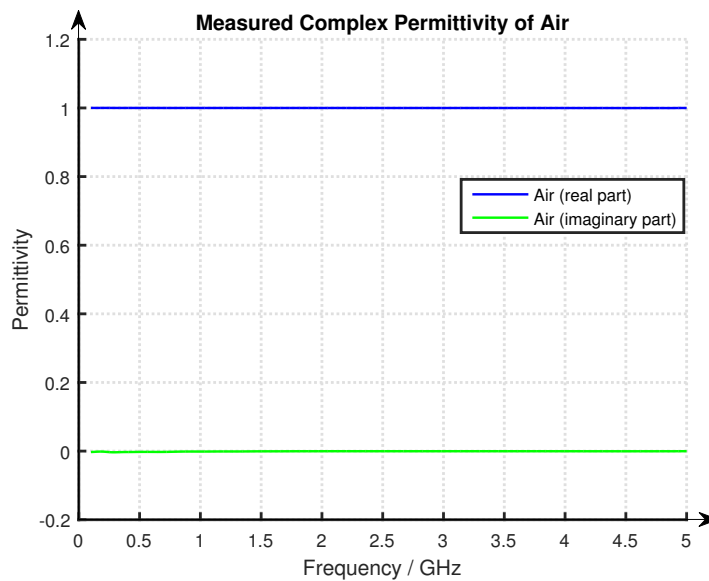
Figure 7.3: Measured permittivity of air.

The real part of the complex permittivity of air is $\epsilon_r = 1$ over the measured frequency interval. The imaginary part are a measure of the losses in the material and for air there are no measurable losses.

To test the algorithm and verify that the measured data is correct, a known case is used. Air has almost the same permittivity as vacuum which is $\epsilon_r = 1$. The real permittivity is one over the measured frequency range and there are no losses which can be seen from the imaginary part of the plot.

Teflon is a reliable test sample due to its known characteristics. A test sample of teflon was milled with the size $150x32x12\text{mm}^3$. Fig. 7.4 shows the measured value of teflon with the TEM cell.

Figure 7.4: Measured permittivity of teflon.

To verify the real measurement a graph with the numerical simulated values of teflon are shown in Fig. 7.5.

Figure 7.5: Numerical permittivity of teflon.

The numerical and the measured values of teflon almost coincides. The differences occur due to the differences between the 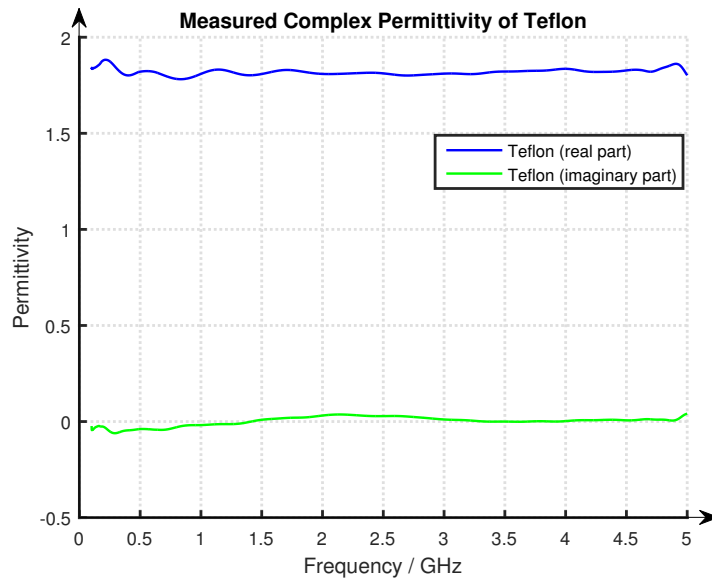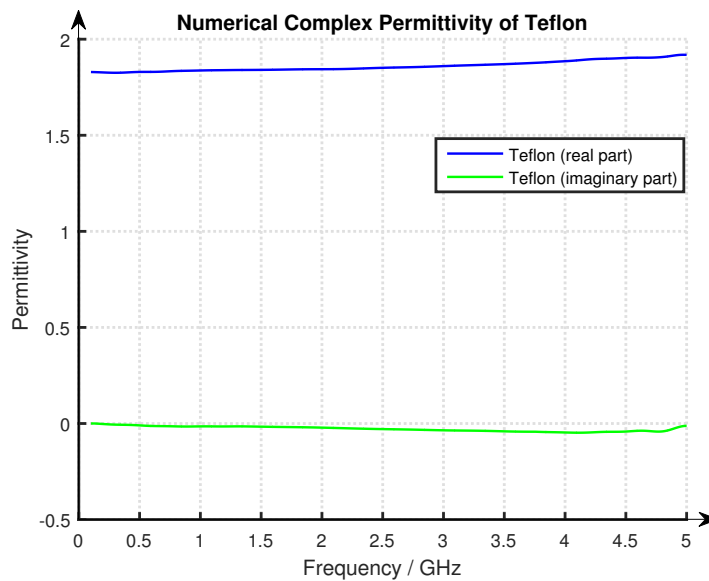manufactured TEM cell and the CAD constructed TEM cell in the numerical environment. The computational time in CST due to high meshing in CST are also a restriction. To perform effective research, an approximate model is constructed in CST with coarser meshing because of the long computational time. The real value of permittivity of Teflon is around $\epsilon_r = 2.1$. The difference between the measured and the real value may be due to signal distortion and electromagnetic field leakage around the test sample. The fact that the TEM cell is not calibrated is also vital for the result. To achieve a better and more accurate result one needs to work with the calibration. It is then important to know the accurate position of the test sample so one can calibrate the reference plane from the port to the test sample surface.

Bakelite is a commonly used material in electronics and can therefore be interesting to investigate. It is prepared from phenol and formaldehyde at high temperature and high pressure, and became the first thermosetting resin. Fig.7.6 shows the permittivity of Bakelite with the size $150x32x12$mm^3.
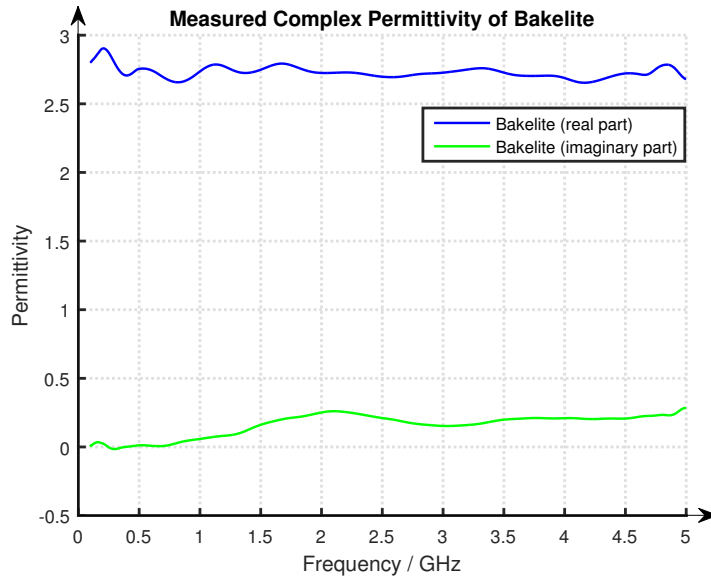
Figure 7.6: Measured permittivity of bakelite.

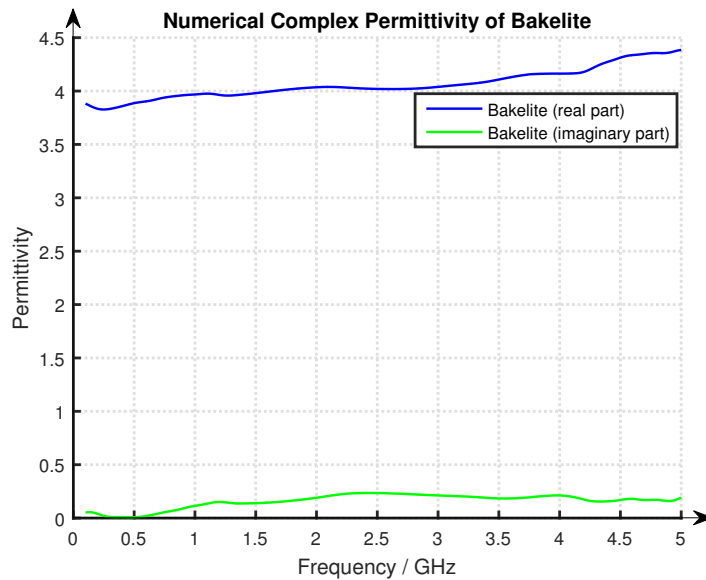Fig. 7.7 shows the simulated values of bakelite.

Figure 7.7: Numerical permittivity of bakelite.

Studying the two different graphs of bakelite shows that the values does not coincides. Bakelite is not a well-defined material compared with teflon, and in

pitched tables sets, bakelite permittivity varies between 3.5-5, which depends on the test sample recipe and manufacturing process. The measured value may also be slightly lower than the real value, caused by the signal distortion and electromagnetic field leakage as for the measured Teflon.

When the TEM cell is tested and verified, a test with an unknown material was made. From the plot, a guess can be made on which material the test sample consists of when looking at known tables from example [41]. Fig. 7.8 shows the result.
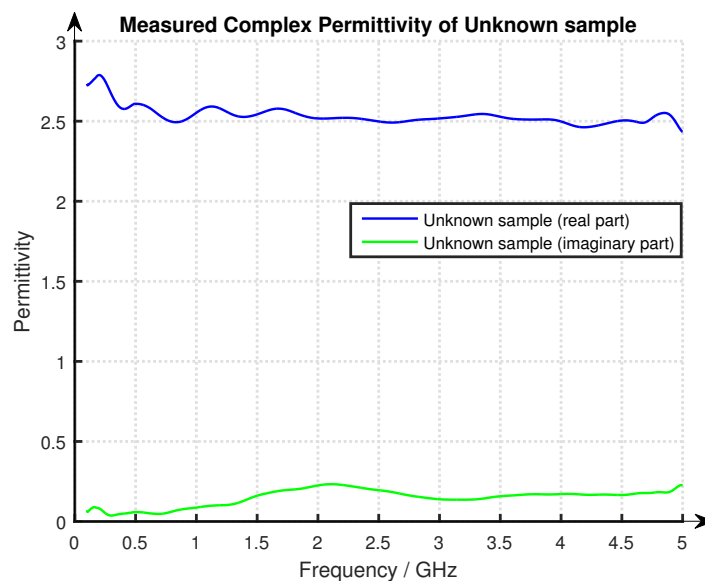
Figure 7.8: Measured permittivity of an Unknown material.

The measured data seems to be relatively smooth over the measured frequency range. Fig. 7.8 indicates that the relative permittivity, $\epsilon_r \approx 2.6$. From the tables and a quick analyze of the material an educated guess can be made resulting in some kind of resin material. Resin is made of different kinds of material where the recipe varies. The mixture of different materials can lead to the permittivity variations given at tabulated data.

7.1   Operating bandwidth test of the TEM cell

After the validation and verification of the results presented in the section above, an operating bandwidth test was made for the TEM cell. As can be seen in Fig. 7.9, the network analyzer was set to 0-10GHz, which shows the scattering parameters.
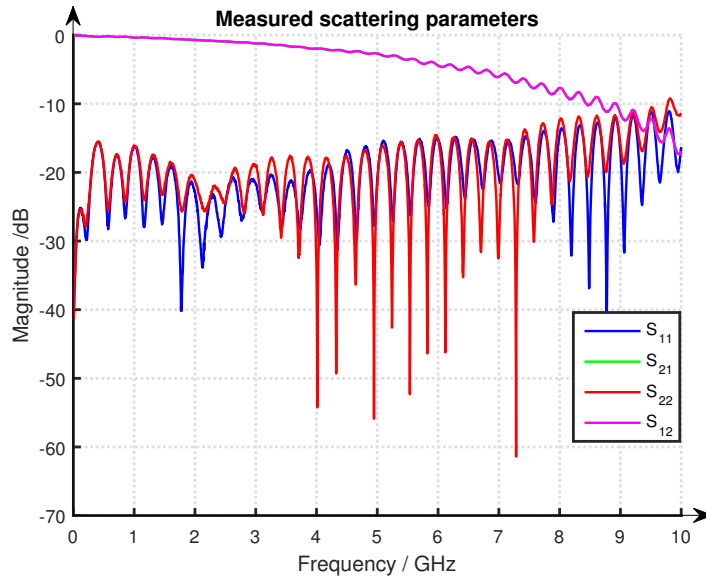
Figure 7.9: Measured scattering parameters of the empty TEM cell.

The numerical values of the S-parameters is presented in Fig. 7.10. It can be seen that the transmission parameters, S_{12} and S_{21} is less damped than the reflection coefficients S_{11} and S_{22}.
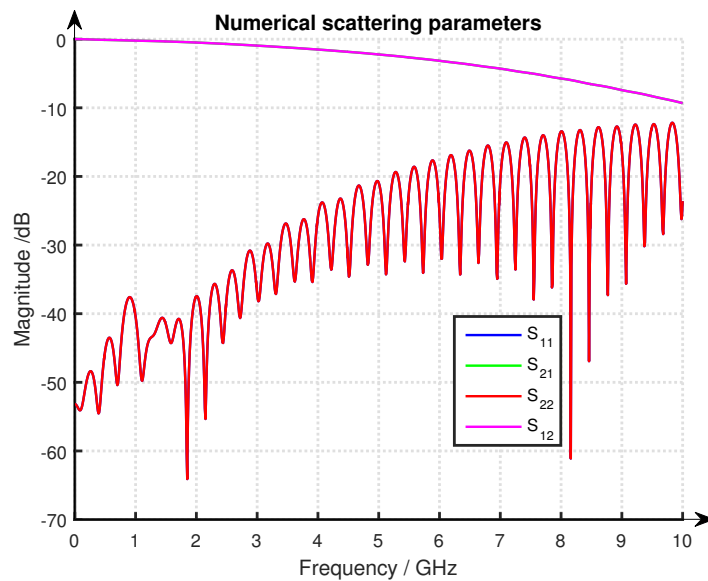
Figure 7.10: Numerical scattering parameters of the empty TEM cell.

Analyzing the measured scattering parameters of an empty TEM cell for a wider frequency spectrum gives an interesting result. The transmission coefficient intersects the reflection coefficient at somewhere around 9GHz. This will lead to an error where the TEM cell and the Baker Jarvis algorithm would not work properly over 9GHz. By studying the numerical values of the S-parameters for the empty TEM cell, this gives an indication that the TEM cell may work for higher frequencies. As described before, the transmission and reflection coefficient is limited to how accurate the measuring setup can be manufactured, which sets an limit of how well it can perform. The TEM cell works for frequencies higher than 5GHz which means that the TEM cell outperforms the given design specification.

The bandwidth test is performed with an empty TEM cell. The data of air is measured and then calculated with Baker Jarvis. Fig. 7.11 shows the permittivity of air for the wider bandwidth test.
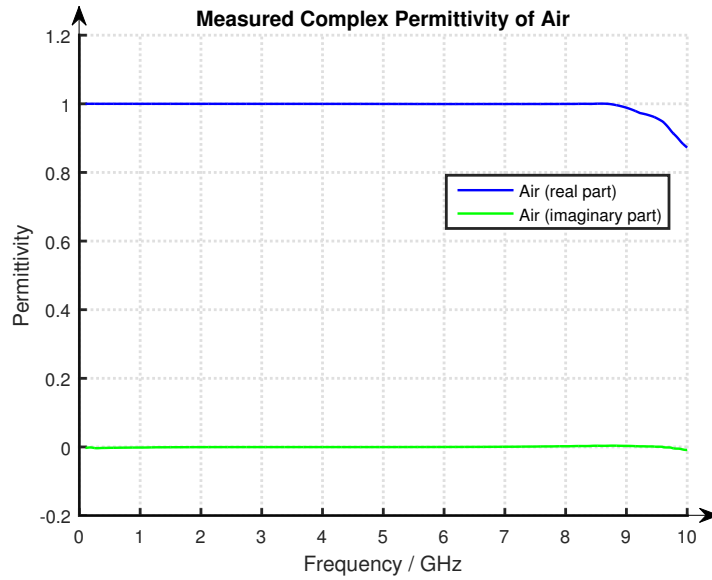
Figure 7.11: Measured permittivity of Air.

From Fig. 7.11 one can see that the TEM cell performs well up to the intersection point 9Ghz. The algorithm gets unstable when the intersection occurs where the data from 9-10GHz is not reliable.

A last bandwidth test is made with teflon. Two different figures represent the in-data of the algorithm, Fig. 7.12, and the processed data is shown in Fig. 7.13
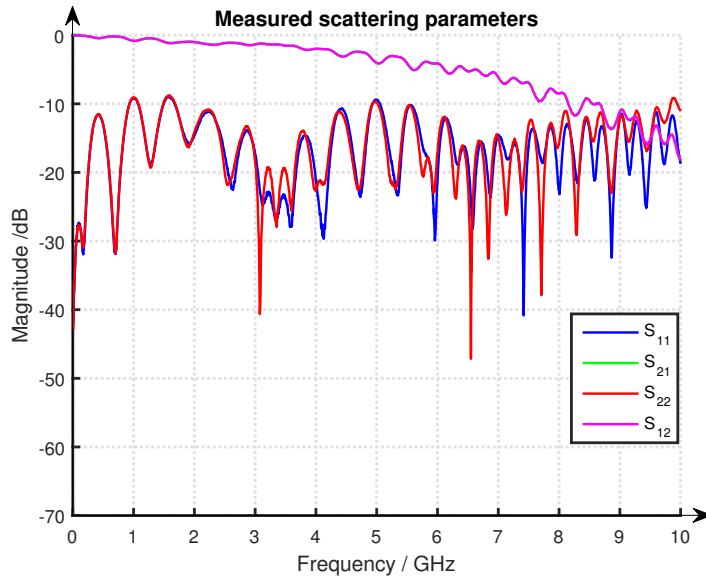
Figure 7.12: Measured scattering parameters of Teflon.
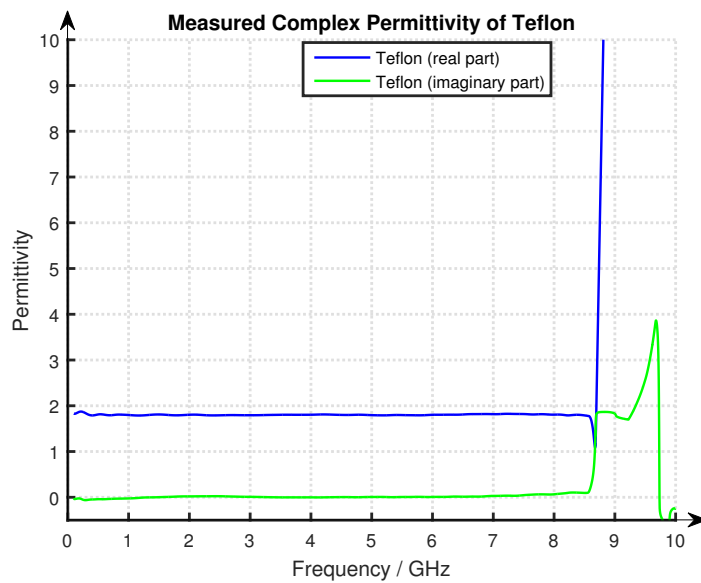
Figure 7.13: Measured permittivity of Teflon.

Analyzing Fig. 7.12 and Fig. 7.13 gives a clear connection between the Baker Jarvis algorithm and the S-parameters at ∼9GHz. The TEM cell performs well up to 9GHz for teflon and gives an upper limit of when reliable values exists. To understand what happens at 9GHz, one needs to dive deeper into the Baker

Jarvis algorithm (2.13) and analyze how the S-parameters is derived and affects the algorithm, which is not further discussed in this thesis.

After the TEM cell was designed and manufactured one major question rose, namely which is the best calibration method for the new type of TEM cell? There are a lot of calibration methods for today's waveguide, but neither of them were particularity developed for the new design. In the development stage of the new model one can explore new calibration methods, a method which is of particular interest is discussed in [8]. The method changes the S-matrix from the calibration reference plane to the test sample reference plane, with an optimization algorithm and then theoretically calculates the complex permittivity and permeability. There is also an interesting algorithm [42] that combines Nicolson-Ross-Weir and the Baker Jarvis algorithm which can be used to improve the measuring result.

The final and the numerically simulated TEM cell can be improved with a better calibration technique as mentioned above and with a refined manufacturing process. Trying to manufacture two identical ports can improve both the reflection and the transmission parameters, which will lead to higher operating bandwidth for the TEM Cell. The measurement results for the given test samples achieved above has a consequent deviation of the permittivity from the real value. If an optimal calibration method was found, the TEM cell could be used to measure complex permittivity for the frequency range 0-8GHz for low permittivity materials.

Chapter 8

Conclusions

There are a lot of aspects that needs to be taken into account while designing this type of waveguide. An open waveguide fixture causes field leakages and refined manufacturing processes of the edges and the surfaces becomes vital for the resulting measurements. Manufacturing a TEM cell of this type requires precision and the geometry of the TEM cell needs to follow the simulated dimensions to get a good matching for the S-parameters. The transition from the coaxial cable to the TEM cell was challenging and considerations in the design part needs to be taken into account to be able to manufacture it. In practice the two ports need to be symmetric to get the same transmission and reflection coefficients of both sides, which is difficult to achieve. The manufacturing of the test sample is important for the accuracy of the measurement and a refined process is crucial to avoid electromagnetic field leakage between the test sample and the conducting plates of the TEM cell.

CST is a numerical computational program which was used in the designing part. The simulation part is necessary while testing new designs of the TEM cell and restrictions in computational power slows down the process. To speed up the design process, a custom computational computer specifically built for the simulation program is highly recommended. The numerical program gives a good hint of the real world and is relatively accurate if handled properly.

The TEM cell works well and with a little more development one can refine the measurements. The electromagnetic field leakage due to the open TEM cell design gives a relatively consistent error in the measurement. After analyzing the three different types of test samples that were used in the measurements, the error can be quantified to 14%. This error can be further investigated to increase the accuracy of the TEM cell. Processing the collected data and filtering it from signals that is leaking around the test sample may increase the accuracy for the measurements. The filtering process can be obtained with for example Fourier Transforms, where the difference in phase shift can be used to decide which signals to be eliminated. Without using a filtering process, and instead considering a compensation factor of 1.14 for the leakage, the TEM cell results in an accuracy within one tenth of a decimal point for the given test sample materials.

The operating bandwidth of the TEM cell was higher than expected. To avoid the higher order modes from propagating, it is important that the surfaces of the conductive plates is as smooth as possible to prevent discontinuities which is triggering the higher order modes. We are not aware of any similar TEM cell design made with microstrip theory and that was challenging. Now the ball is rolling and a first edition of a TEM cell, inspired by a microstrip, is manufactured. Let's see how accurate this design can become in the future.

References

[1] K. L. Shlager, G. S. Smith, and J. G. Maloney. Accurate analysis of tem horn antennas for pulse radiation. *IEEE Transactions on Electromagnetic Compatibility*, 38(3):414–423, Aug 1996. ISSN 0018-9375. doi: 10.1109/15.536071.

[2] J. C. Tippet and D. C. Chang. Radiation characteristics of electrically small devices in a tem transmission cell. *IEEE Transactions on Electromagnetic Compatibility*, EMC-18(4):134–140, Nov 1976. ISSN 0018-9375. doi: 10.1109/TEMC.1976.303492.

[3] T. Mandic, R. Gillon, B. Nauwelaers, and A. Baric. Characterizing the tem cell electric and magnetic field coupling to pcb transmission lines. *IEEE Transactions on Electromagnetic Compatibility*, 54(5):976–985, Oct 2012. ISSN 0018-9375. doi: 10.1109/TEMC.2012.2193888.

[4] K. Malaric and I. Bacic. Efficiency of the materials used in building tem-cell. In *Microwave Techniques, 2008. COMITE 2008. 14th Conference on*, pages 1–3, April 2008. doi: 10.1109/COMITE.2008.4569957.

[5] Sandeep M. Satav and Vivek Agarwal. Do-it-yourself fabrication of an open tem cell for emc pre-compliance. *EMI-EMC Center RCI and Dept. of Electrical Engineering, Indian Institute of Technology-Bombay*, 2008.

[6] C. Iftode, S. Miclaus, P. Bechet, and E. Surducan. A tem cell model analysis for radiofrequency dosimetry improvement by computational means. In *Advanced Topics in Electrical Engineering (ATEE), 2011 7th International Symposium on*, pages 1–4, May 2011.

[7] M. Borsero, G. Vizio, D. Parena, and V. Teppati. Synthetic tdr measurements for tem and gtem cell characterization. *IEEE Transactions on Instrumentation and Measurement*, 56(2):271–274, April 2007. ISSN 0018-9456. doi: 10.1109/TIM.2007.890796.

[8] R. Tumayan, X. Bunlon, A. Reineix, G. Andrieu, and C. Guiffaut. A method using an open tem cell to extract the complex permittivity of an unknown material. In *2014 International Symposium on Electromagnetic Compatibility*, pages 1102–1106, Sept 2014. doi: 10.1109/EMCEurope.2014.6931067.

[9] S.   J.   Orfanidis.   *Electromagnetic   Waves   and   Antennas.*
      www.ece.rutgers.edu/ orfanidi/ewa, 1999-2014.

[10] M. Yarleque and A. Miranda. Permittivity measuring technique based on
      a parallel-plate waveguide concept. In *Andean Region International Con-
      ference (ANDESCON), 2012 VI*, pages 67–70, Nov 2012. doi: 10.1109/An-
      descon.2012.25.

[11] A. Kazemipour, D. Allal, A. Litwin, and M. Bourghes. Wideband tem
      parallel-plate cell for sar-probe calibration. In *CPEM 2010*, pages 710–711,
      June 2010. doi: 10.1109/CPEM.2010.5543503.

[12] Standard test method for measuring relative complex permittivity and rela-
      tive magnetic permeability of solid materials at microwave frequencies us-
      ing waveguide. *ASTM International*, 10.02, 2008. doi: 10.1520/D5568-14.

[13] S. K. Yee, A. Sayegh, A. Kazemipour, and M. Z. M. Jenu. Design and calibra-
      tion of a wideband tem-cell for material characterization. In *2012 Asia-Pacific
      Symposium on Electromagnetic Compatibility*, pages 749–752, May 2012. doi:
      10.1109/APEMC.2012.6237852.

[14] S. Hilavin and A. Kustepeli. Design and implementation of a tem stripline
      for emc testing. *IEEE Transactions on Electromagnetic Compatibility*, 56(1):23–
      27, Feb 2014. ISSN 0018-9375. doi: 10.1109/TEMC.2013.2271834.

[15] M. L. Crawford. Generation of standard em fields using tem transmission
      cells. *IEEE Transactions on Electromagnetic Compatibility*, EMC-16(4):189–195,
      Nov 1974. ISSN 0018-9375. doi: 10.1109/TEMC.1974.303364.

[16] P. F. Wilson and M. T. Ma. Simple approximate expressions for higher or-
      der mode cutoff and resonant frequencies in tem cells. *IEEE Transactions on
      Electromagnetic Compatibility*, 28(3):125–130, Aug 1986. ISSN 0018-9375. doi:
      10.1109/TEMC.1986.4307269.

[17] C. Rostamzadeh, B. Archambeault, and S. Connor. Fdtd analysis of sym-
      metric tem cell. In *2005 International Symposium on Electromagnetic Compat-
      ibility, 2005. EMC 2005.*, volume 2, pages 525–529 Vol. 2, Aug 2005. doi:
      10.1109/ISEMC.2005.1513571.

[18] John H. Grosvenor Jr. Richard G.Geyer James Baker-Jarvis, Michael
      D. Janezic. *Transmission/Reflection and Short-Circuit Line Methods for Measur-
      ing Permittivity and Permeability.* NIST, 1992.

[19] A. M. Nicolson and G. F. Ross. Measurement of the intrinsic properties
      of materials by time-domain techniques. *IEEE Transactions on Instrumen-
      tation and Measurement*, 19(4):377–382, Nov 1970. ISSN 0018-9456. doi:
      10.1109/TIM.1970.4313932.

[20] P. Queffelec, P. Gelin, J. Gieraltowski, and J. Loaec. A microstrip device for
      the broad band simultaneous measurement of complex permeability and

permittivity. *IEEE Transactions on Magnetics*, 30(2):224–231, Mar 1994. ISSN 0018-9464. doi: 10.1109/20.312262.

[21] Constantine A. Balanis. *Advanced Engineering Electromagnetics*. John Wiley & Sons, 1989.

[22] C.P. Neo V.V. Varadan V.K. Varadan L.F. Chen, C.K. Ong. *Microwave Electronics measurement and materials characterisation*. John Wiley & Sons, 2004.

[23] E. KiliÃğ, U. Siart, C. H. Schmidt, and T. F. Eibert. Dielectric material measurements supported by electromagnetic field solvers. In *General Assembly and Scientific Symposium, 2011 URSI*, pages 1–4, Aug 2011. doi: 10.1109/URSIGASS.2011.6050289.

[24] J. Baker-Jarvis, E. J. Vanzura, and W. A. Kissick. Improved technique for determining complex permittivity with the transmission/reflection method. *IEEE Transactions on Microwave Theory and Techniques*, 38(8):1096–1103, Aug 1990. ISSN 0018-9480. doi: 10.1109/22.57336.

[25] L. P. Ligthart. A fast computational technique for accurate permittivity determination using transmission line methods. *IEEE Transactions on Microwave Theory and Techniques*, 31(3):249–254, Mar 1983. ISSN 0018-9480. doi: 10.1109/TMTT.1983.1131471.

[26] Jin Au Kong David H. Staelin, Ann W. Morgenthaler. *Electromagnetic Waves*. Prentice-Hall, 1994.

[27] David K. Cheng. *Field and Wave Electromagnetics, Second Edition*. Addison-Wesley Publishing Company, 1989.

[28] N.Marcuvitz. *Waveguide Handbook*. McGraw-Hill Book Company, 1951.

[29] David M. Pozar. *Microwave Engineering, Third edition*. John Wiley & Sons, 2005.

[30] Robert E. Collin. *Foundations for Microwave Engineering, second edition*. John Wiley & Sons, 2001.

[31] Inder Bahl Prakash Bhartia K.C. Gupta, Ramesh Garg. *Microstrip Lines and Slotlines*. Artech House, 1996.

[32] E. Hammerstad and O. Jensen. Accurate models for microstrip computer-aided design. In *Microwave symposium Digest, 1980 IEEE MTT-S International*, pages 407–409, May 1980. doi: 10.1109/MWSYM.1980.1124303.

[33] J. D. Kraus. *Antennas, Second Edition*. McGraw-Hill, New York, 1988.

[34] R. W. Klopfenstein. A transmission line taper of improved design. *Proceedings of the IRE*, 44(1):31–35, Jan 1956. ISSN 0096-8390. doi: 10.1109/JRPROC.1956.274847.

[35] Standard test method for measuring relative complex permittivity and relative magnetic permeability of solid materials at microwave frequencies using coaxial air line. *ASTM International*, 10.02(STD-70595), 2008. doi: 10.1520/D7449_D7449M-08.

[36] Dr. R. L. Eisenhart. A better microstrip connnector. *Microwave Symposium Digest, 1978 IEEE-MTT-S International*, 23:318–320, Jun 1978.

[37] J. C. Cheng, E. S. Li, W. F. Chou, and K. L. Huang. Improving the high-frequency performance of coaxial-to-microstrip transitions. *IEEE Transactions on Microwave Theory and Techniques*, 59(6):1468–1477, June 2011. ISSN 0018-9480. doi: 10.1109/TMTT.2011.2123911.

[38] M. Shahabadi G. Askari, M. Kamarei and H. M. Sadeghi. Analysis, design and implementation of a broadband coaxial-to-microstrip transition for uwb radars. *PIERS Proceedings*, (8):972–977, aug 2014.

[39] R. E. Collin. The optimum tapered transmission line matching section. *Proceedings of the IRE*, 44(4):539–548, April 1956. ISSN 0096-8390. doi: 10.1109/JRPROC.1956.274938.

[40] S. A. P. Rizvi and R. A. A. Khan. Klopfenstein tapered 2 # x2013;18 ghz microstrip balun. In *Proceedings of 2012 9th International Bhurban Conference on Applied Sciences Technology (IBCAST)*, pages 359–362, Jan 2012. doi: 10.1109/IBCAST.2012.6177579.

[41] Roald K. Wangsness. *Electromagnetic fields*. John Wiley & Sons, 1986.

[42] K. Chalapat, K. Sarvala, J. Li, and G. S. Paraoanu. Wideband reference-plane invariant method for measuring electromagnetic parameters of materials. *IEEE Transactions on Microwave Theory and Techniques*, 57(9):2257–2267, Sept 2009. ISSN 0018-9480. doi: 10.1109/TMTT.2009.2027160.

[43] Saab. Gripen e roll out. http://mediaportal.saabgroup.com/, May 2016.

[44] Todd Helmenstine. Periodic table of the elements. www.sciencenotes.org, 2014.

[45] Göran Jönsson. Lund university lecture amplified design. In *RF Amplified Design*, page 3, Dec 2014.